UiT
THE ARCTIC
UNIVERSITY
OF NORWAY

Department of Physics and Technology

Modeling Ice-shelf Ocean Interaction at Petermann Glacier, Greenland

—

Weiyang Bao

FYS-3900 Master's Thesis in Physics

May 2017

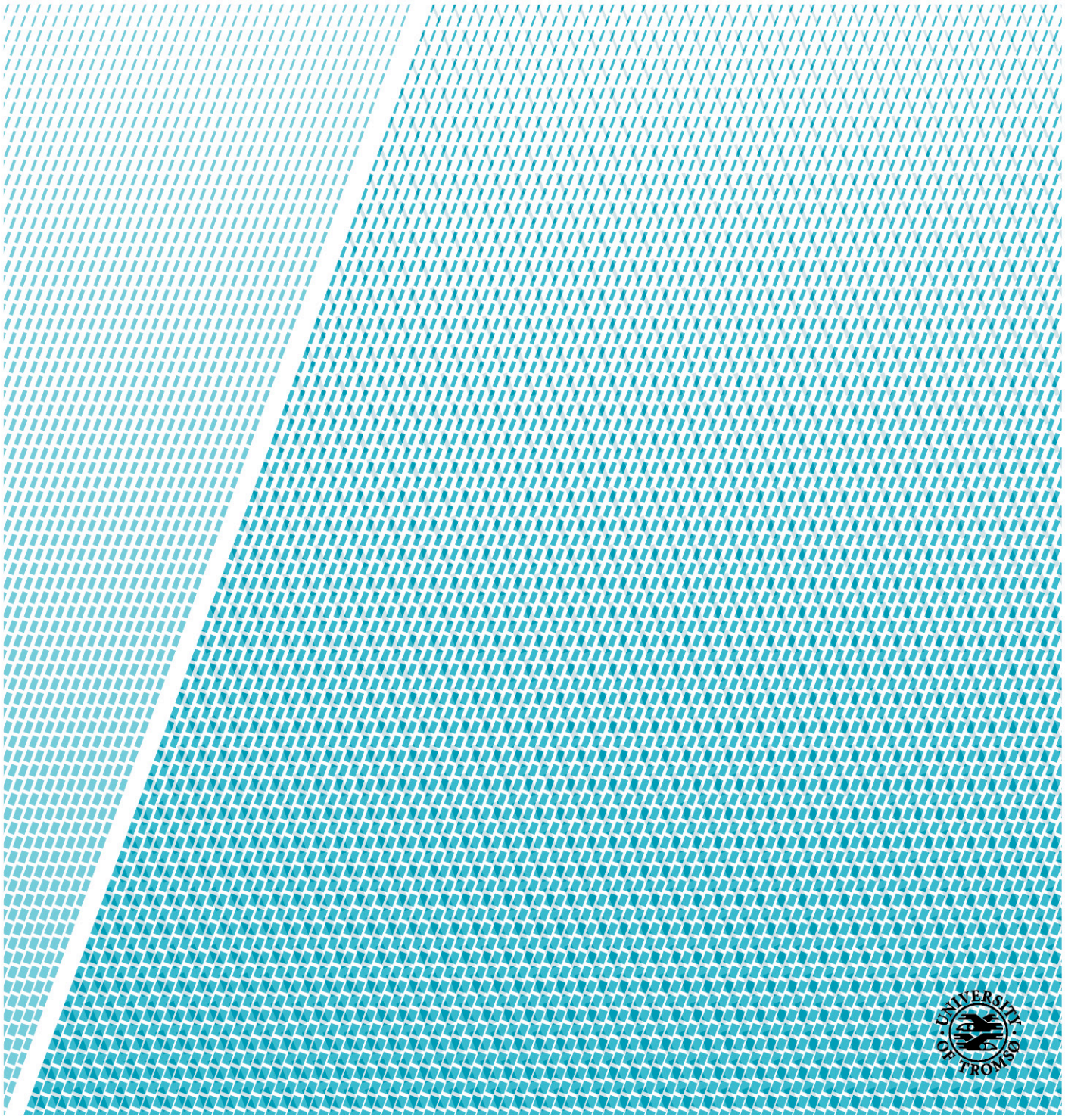

Abstract

Petermann Glacier drains about 4% of the Greenland ice sheet area, with at least 80% of its mass loss through basal melting of the floating ice shelf. Utilizing a high-resolution coupled ice-shelf-ocean model, we aim at understanding the ocean circulation in Nares Strait and the mechanism of oceanic heat supply below the ice shelf as well as quantifying the basal mass loss. The numerical model is based on the Finite-Volume Community Ocean Model (FVCOM), taking advantage of its flexible spatial resolution that can follow the topography. A regional model domain has been set up, which spans the greater Nares Strait region and covers Petermann Fjord with 200-m horizontal resolution and includes the Petermann Glacier geometry. As a first step, we focus on the role of tides for transporting ocean water into the ice-shelf cavity. Tidal simulations are validated with available observations, demonstrating the capability of FVCOM in reproducing the tidal current pattern in Nares Strait. Lagrangian particle trajectories are computed to explore the water exchange in Petermann Fjord. It is found that tidal oscillations in Nares Strait lead to a residual circulation in the fjord and inside the ice-shelf cavity. These results suggest that tidal dynamics plays an important role in modulating regional circulation in Petermann Fjord and heat transport to Petermann Ice Shelf.

Acknowledgements

This thesis work has comprised my most memorable experience in Tromsø, this lovely city in the Arctic, and I am really grateful for many those who have supported and helped me throughout my stay here. Foremost, I would like to express my sincere gratitude to my supervisors Tore Hattermann, Rune Graversen and Guoping Gao for all their guidance. With his expertise, insight, enthusiasm and preciseness, Tore has set the best example of a physical oceanographer for me. His great patience and encouragement has helped me through the toughest of times. Thanks to all those enlightening conversations with Rune and his valuable suggestions, I finally get this finishing touch on my thesis. I would also like to thank Prof. Guoping Gao at Shanghai Ocean University, for his supportive and encouraging supervision from the beginning of my graduate study.

I also owe my deep gratitude to Akvaplan-niva, which has provided a precious office space, a vivid research environment and more importantly so many great colleagues for me. I cannot be more thankful to Qin, for she has brought not only huge help in my work but great care for life. I also really appreciate the scientific help and support in our modeling work from the oceanography group, especially Eli and Hans Kristian. In addition, I would like to thank Chris, Hector and all those awesome friends for every exciting and interesting basketball game we had.

A special thank you must go to my second home in the Arctic. Kjeld, Trude, Endre and our best kitty friend Dinyo, your optimistic attitude toward life has deeply infected with me. I will never forget those happy memories when we lived together and accompanied each other.

Lastly and most of all, I am forever indebted to my parents, who have always been there for me with their selfless and permanent love. You have raised me up to more than I can be. And my beloved Yu, our expeditions throughout many places always remind me that there is more to life than work. You have made my life truly sweet and enjoyable, thank you!

Financial support for the research in this thesis from the Research Council of Norway (RCN) through the “Modeling ice shelf basal melting below the floating ice shelf of Petermann Glacier” project (No. 263855/H30) is gratefully acknowledged.

Contents

List of Tables

List of Figures

1 Introduction

Over the last two decades, mass loss from the Greenland ice sheet has increased rapidly. The loss rate has arrived at a 6-cm equivalent global sea level rise within one hundred years [*Vaughan et al.*, 2013], whilst the poor bounds on this rate bring the largest uncertainty to global sea level change projections [*Shepherd et al.*, 2012]. The greatest mass loss of the Greenland ice sheet occurs at marine-terminating outlet glaciers, with a major contribution from increased oceanic heat flux to the glacier fronts and margins [*Straneo & Heimbach*, 2013]. As a result, the collapse of ice shelves and retreat of grounding lines occurred frequently at these places [*Pritchard et al.*, 2009]. As the oceanic heat transfer depends on exchange at fjord mouths, flow over sills and ice-ocean boundary dynamics [*Shroyer et al.*, 2017], it is necessary to better understand these processes before estimating the projected sea level rise.

Petermann Glacier (81 °N, 61 °W) is a major outlet glacier in northwest Greenland and features the second largest floating ice shelf in the Northern Hemisphere [*Münchow et al.*, 2016]. The glacier is connected to Nares Strait through Petermann Fjord, and Nares Strait is connected to the Arctic Ocean in the north and the Atlantic Ocean via Baffin Bay in the south (Fig. 1.1). Petermann Glacier drains about 4% of the Greenland ice sheet area via a network of glacial channels and landward [*Bamber et al.*, 2013]. Basal melting is thought to be responsible for at least 80% of its mass loss since the ice shelf interacts directly with the ocean [*Rignot & Steffen*, 2008]. Therefore, understanding the ice-shelf-ocean interaction at the base is important for predicting the stability of the Petermann Glacier as well as the Greenland ice sheet.

Figure 1.1: The geographical location of Petermann Glacier. From NASA MODIS image.

As a key passageway for freshwater and heat exchange between the Arctic Ocean and the sub-arctic North Atlantic seas, Nares Strait is dominated by tidal dynamics [*Davis*, 2015]. Investigating the tidal characteristics and effects is thus our first step to understand ocean circulation and properties in Nares Strait and Petermann Fjord in addition to the mechanism of oceanic heat transport towards the floating ice shelf. Here, we use a fully coupled barotropic regional model augmented by a fixed-geometry ice shelf to show how the ocean's response to tidal dynamics in Nares Strait affects basal melting of Petermann Ice Shelf.

1.1 Related work

The rapid development of modern observations has largely extended the explorations for Petermann Glacier. These new observations identify the Petermann ice-ocean system as a dynamically rich and rapidly changing environment, although the dynamical implications are not fully understood [*Münchow et al.*, 2016]. Early in 1990s, measurements from radar interferometry found that nearly the entire glacier section below its grounding line underwent tidal motion, which caused the hinge-line (the limit of tidal flexing of the glacier) migration, but further studies are needed to determine the oceanographic conditions that induced the basal melting [*Rignot*, 1996, 1998]. Recent observational programs such as the Arctic Sub-Arctic Ocean Flux (ASOF) experiment investigated the seawater flux through Nares Strait to the Arctic Ocean. The 2003-06 measurements of currents showed that the flow was dominated by mixed diurnal and semi-diurnal tidal currents [*Münchow et al.*, 2006; *Münchow & Melling*, 2008]. Analyses of these measurements by *Davis* [2015] demonstrated that tides in Nares Strait served as a major contributor to the regional circulation. All these have provided important information of the ocean dynamic environment around the glacier's terminus.

In quantifying the mass loss below Petermann ice shelf, *Rignot and Steffen* [2008] mapped the steady-state for the ice shelf. They found that ~80% of the mass loss occurred through basal melting, creating sub-ice-shelf channels as well. *Gladish et al.* [2012] developed a numerical model for an interacting ice shelf and ocean. The generated basal melt rates ranged from 25 m/yr at the grounding line to zero at the ice front. Later the interannual changes of the ice shelf from 2000 to 2012 were documented from remote sensing observations [*Münchow et al.*, 2014]. The calculated along-flow ice divergence in the steady-state represented 6.3 Gt/yr mass loss through basal melting (~5 Gt/yr). It was suggested that the thinning basal channels weakened the structure of ice shelf and were responsible for large iceberg-calving events.

The ice-shelf-ocean interaction is one of the leading causes for the retreat of glaciers [*Straneo et al.*, 2013]. *Johnson et al.* [2011] discussed the regional oceanography of Petermann Fjord with the first oceanographic measurements made in the fjord. Their results indicated that not merely heat input from the Atlantic water, other factors including winter mixed layer depth, mobile versus landfast sea ice cover and fjord geometry were also important to ice-shelf melting. A retreating ice front also changed ocean circulation within the fjord. Ocean observations in Nares Strait and Petermann Fjrod from 2012 to 2016 showed that Atlantic-sourced ocean waters below Petermann Ice Shelf became warmer and saltier, indicating a potential for large changes in ice-ocean thermodynamic interactions [*Münchow et al.*, 2016]. The latest results from a high-resolution coupled ocean and sea-ice model suggested that seasonal shifts in the sea-ice cover in Nares Strait might induce ocean circulation change [*Shroyer et*

al., 2017]. Under summer mobile sea ice, warm waters are upwelled on the eastern side of the strait and enter Petermann fjord, thus enhancing basal melting. While in winter under landfast sea-ice condition, cold near-surface waters are maintained on the eastern side of the strait and within the fjord, reducing basal melting and insulating the ice shelf.

Apart from the sea-ice mechanism that affects the interaction between the ocean water and the ice shelf, the role of tides in Nares Strait for water exchange with Petermann Fjord has not previously been studied. We are therefore motivated to simulate the regional tidal dynamics using the FVCOM with an unstructured grid.

1.2 Thesis layout

The thesis is structured in six chapters. Chapter 2 briefly introduces the theoretical foundation of FVCOM, including its governing equations, boundary conditions and grid properties. How the initial setup of the model is configured and the input is preprocessed are also included.

In Chapter 3, the basic theory behind ocean tides is explained with the causes of tides and tidal constituents. This chapter also includes the principles of tidal analysis and prediction, alongside a brief description of the MATLAB package T_TIDE used in this study.

The next chapter introduces the 2-D cases used to validate model results: one is the Pressure Gradient Error test, the other is the tidal simulation. The comparison of tides and tidal currents in Nares Strait between modeled results and observations is also discussed.

The following Chapter 5 presents the results from the Lagrangian particle seeding experiment at three different cross-sections in the model domain. Both calculation of particle tracking and water exchange characteristics are represented accompanied with a brief discussion of the results.

At last, in Chapter 6, the conclusion and suggestions to further work are presented.

2 FVCOM theoretical foundation and configuration

2.1 Introduction of FVCOM

The unstructured-grid Finite-Volume Community Ocean Model (FVCOM) is a fully coupled ice-ocean-wave-sediment-ecosystem model system [*Chen et al.*, 2003]. It combines finite-element methods for geometric flexibility and finite-difference methods for simple discrete structures and computational efficiency. This numerical approach also provides an accurate representation of mass, momentum, salt, and heat conservation in coastal and estuarine regions with complex geometry. The conservative nature of FVCOM in addition to its flexible grid topology and code simplicity make FVCOM ideally suited for interdisciplinary application in the coastal ocean, including the region of our focus.

2.1.1 Governing equations

The primitive equations in Cartesian coordinates consist of the following:

momentum equations (in 2-D modeling)

$$\frac{\partial u}{\partial t} + u\frac{\partial u}{\partial x} + v\frac{\partial u}{\partial y} + w\frac{\partial u}{\partial z} - fv = -\frac{1}{\rho_0}\frac{\partial P}{\partial x} + \frac{\partial}{\partial z}\left(K_m\frac{\partial u}{\partial z}\right) + F_u \tag{2-1}$$

$$\frac{\partial v}{\partial t} + u\frac{\partial v}{\partial x} + v\frac{\partial v}{\partial y} + w\frac{\partial v}{\partial z} + fu = -\frac{1}{\rho_0}\frac{\partial P}{\partial y} + \frac{\partial}{\partial z}\left(K_m\frac{\partial v}{\partial z}\right) + F_v \tag{2-2}$$

continuity equation

$$\frac{\partial u}{\partial x} + \frac{\partial v}{\partial y} + \frac{\partial w}{\partial z} = 0 \tag{2-3}$$

temperature equation

$$\frac{\partial T}{\partial t} + u\frac{\partial T}{\partial x} + v\frac{\partial T}{\partial y} + w\frac{\partial T}{\partial z} = \frac{\partial}{\partial z}\left(K_h\frac{\partial T}{\partial z}\right) + F_T \tag{2-4}$$

salinity equation

$$\frac{\partial S}{\partial t} + u\frac{\partial S}{\partial x} + v\frac{\partial S}{\partial y} + w\frac{\partial S}{\partial z} = \frac{\partial}{\partial z}\left(K_h\frac{\partial S}{\partial z}\right) + F_s \tag{2-5}$$

and density equation

$$\rho = \rho(T, S) \tag{2-6}$$

where x, y, z are the east, north and vertical axes in the Cartesian coordinate system; u, v, w are the x, y, z velocity components; T is the temperature; S is the salinity; ρ is the density; P is the pressure; f

is the Coriolis parameter; g is the gravitational acceleration; K_m is the vertical eddy viscosity coefficient; K_h is the thermal vertical eddy diffusion coefficient; and F_u, F_v, F_T, F_S represent the horizontal momentum, thermal and salt diffusion terms [*Chen et al.*, 2013].

In the vertical, FVCOM applies the σ-coordinate system (also allow for various choices), at which all layers are uniformly divided. This terrain-following coordinate is defined as:

$$\sigma = \frac{z-\zeta}{H+\zeta} = \frac{z-\zeta}{D} \tag{2-7}$$

where H is the bottom depth (relative to $z = 0$); ζ is the height of the free surface (relative to $z = 0$) and $D = H + \zeta$ is the total water column depth. See the FVCOM user manual [*Chen et al.*, 2013] for the transformation of Eq. (2-1)~(2-7) in the terrain-following coordinate.

2.1.2 Boundary conditions

The initial condition of the model is zero velocity and zero surface elevation. In the σ-coordinate system, velocity variation at the free surface ($\sigma \to 0$) is represented as:

$$\left(\frac{\partial \mathrm{u}}{\partial \sigma}, \frac{\partial \mathrm{v}}{\partial \sigma}\right) = \frac{J}{\rho_0 K_m}\left(\tau_{sx}, \tau_{sy}\right), \omega = 0; \tag{2-8}$$

where $\left(\tau_{sx}, \tau_{sy}\right)$ are the x and y components of surface wind stresses; $J = \frac{\partial z}{\partial \sigma}$; ω is the transformed vertical velocity.

The computation at the open boundary is driven by surface elevation from tides, which are obtained from the harmonic constants of eight major tidal constituents (from Section 3.1). Initial phases and amplitudes of the tide waves at the open boundaries are taken from an Arctic Ocean model named AOTIM [*Padman & Erofeeva*, 2004]. In our 2-D modeling, the density is constant because of the integration over the entire depth. The pressure gradient in the σ-coordinate system will be very small, hence the vertical acceleration can be neglected. Including the continuity equation (2-3), the evolution of the flow in a tidal current can be described by:

$$\frac{Du}{Dt} + \frac{1}{\rho}\frac{\partial p}{\partial x} - fv = F_x \tag{2-9}$$

$$\frac{Dv}{Dt} + \frac{1}{\rho}\frac{\partial p}{\partial x} + fu = F_y \tag{2-10}$$

$$\frac{1}{\rho}\frac{\partial p}{\partial z} + g = 0 \tag{2-11}$$

which are the x, y and z components of the momentum equation respectively, and Eq. (2-11) also represents the hydrostatic balance of pressure in depth [*Marshall & Plumb*, 2016].

2.1.3 Unstructured triangle grids

The horizontal numerical computational domain is subdivided into a set of non-overlapping unstructured triangular cells. An unstructured triangle is comprised of three nodes, a centroid, and three sides (Fig. 2.1).

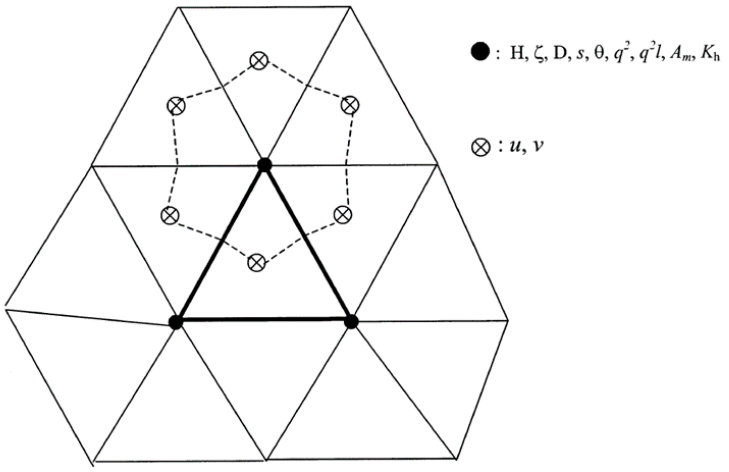

Figure 2.1: The unstructured grid for the finite-volume model.

In order to accurately estimate the sea-surface elevation, currents and salt and temperature fluxes, u and v are placed at the centroids and all scalar variables (e.g. $\zeta, H, D, \omega, S, T, \rho, K_m, K_h$) are placed at the nodes. Scalar variables at each node are determined by a net flux through the sections linked to centroids and the mid-point of the adjacent sides in the surrounding triangles, while u and v are calculated based on a net flux through the three sides of that triangle [*Chen et al.*, 2013].

2.1.4 Ice-shelf geometry

Here we use a version of FVCOM that has been augmented the ice shelf of Petermann Glacier to include sub-ice-shelf cavities. Two cross-sections are set to present the geometry beneath the floating ice shelf (Fig. 2.2). The evolutions of smoothed ice thickness and bathymetry (smoothing method in Section 2.2.2) along each section are shown in Figure 2.3. The bathymetry in our model consists of the water column thickness (WCT, the distance from the seabed to the ice-shelf base) and the Petermann Glacier ice draft geometry. The original WCT comes from International Bathymetric Chart of the Arctic Ocean (IBCAO) version 3.0 1-km grid data [*Jakobsson et al.*, 2012]. The ice draft geometry is provided by the ice thickness data obtained from IceBridge BedMachine Greenland version 2 [*Morlighem et al.*, 2015], which has a spatial resolution of 150 m.

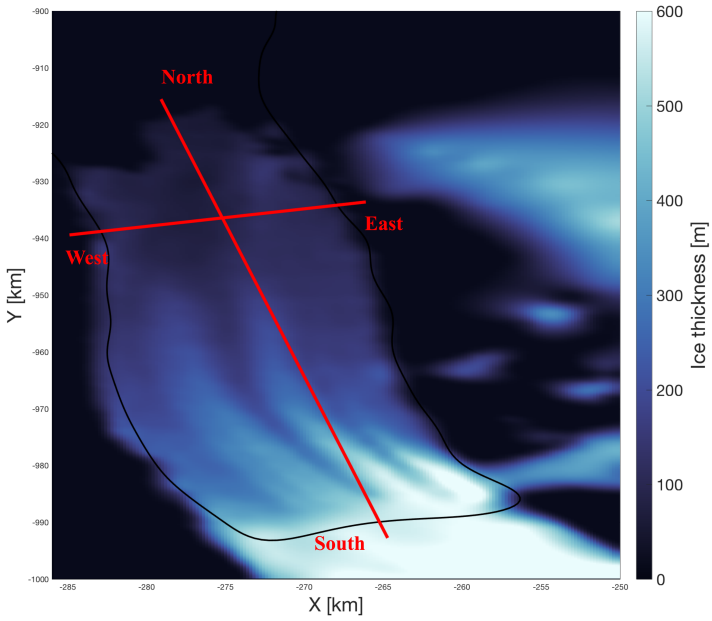

Figure 2.2: The cross-sections (in red lines) of Petermann Ice Shelf.

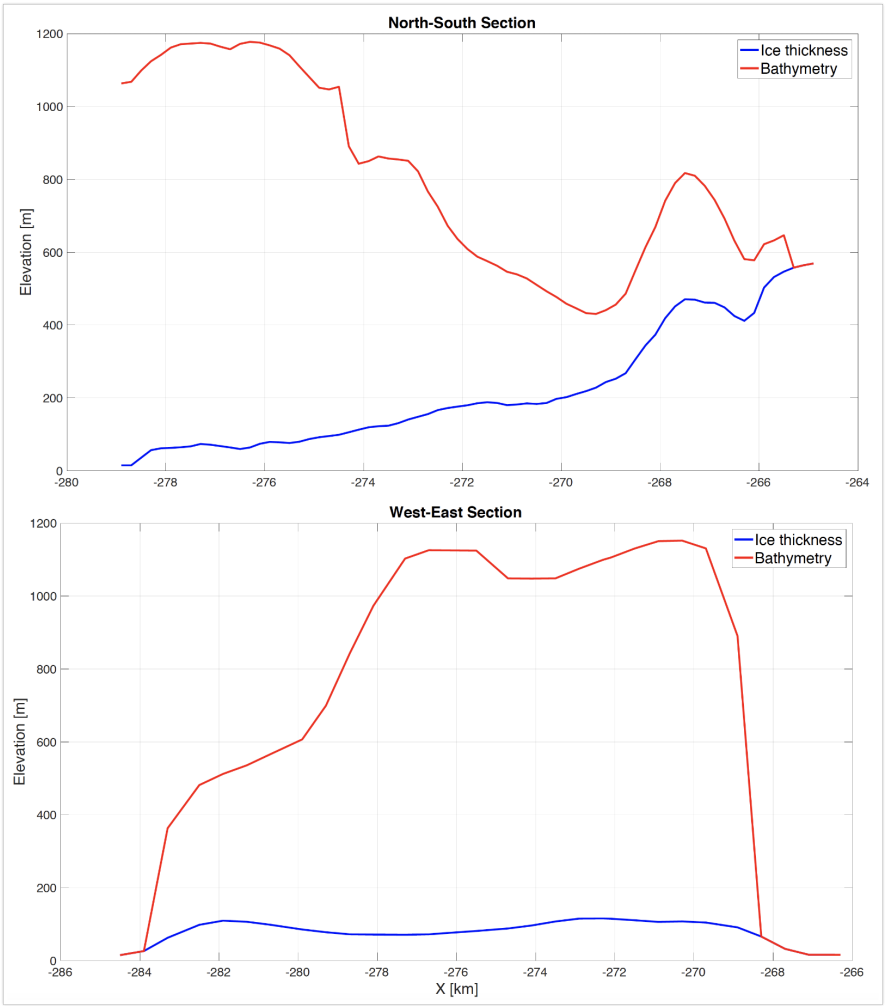

Figure 2.3: Evolutions of ice thickness and bathymetry along cross-sections.

In the landward (north-south) direction, the bathymetry decreases as ice gets thicker, but they get equal at last, which indicates the location of the grounding line. In the west-south direction, the ice-shelf base exhibits a channelized morphology of cavity, which is initiated by irregularities in the ice along the grounding line and then enlarged by ocean melting [*Gladish et al.*, 2012]. Nevertheless, the three-dimensional module in the current model version is still under development, which has been limiting the scope of this study to 2-D tidal simulation.

2.2 Model configurations

2.2.1 Computational domain and grid design

The computational domain locates in the range of 74°N~89°N, 85°W~20°W, mainly covering Nares Strait and Petermann Fjord (Fig. 2.4). Two open boundaries are set to investigate impacts from the Atlantic inflow in the north and extension of the oceanic flow to the south in Baffin Bay.

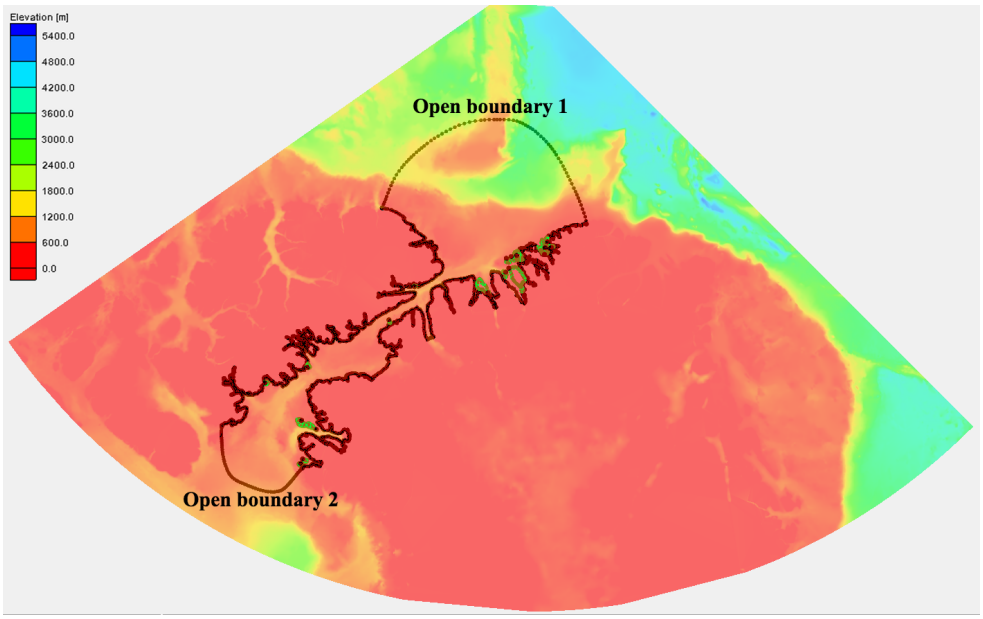

Figure 2.4: Model domain outlined in a background of water surface elevation relative to the seabed.

An efficient method for generating unstructured and triangular meshes is DistMesh [*Persson & Strang*, 2004] that is available in MATLAB code. It applies a simple algorithm that combines a physical principle of force equilibrium in a 2-D truss structure (a structure of springs) with a mathematical representation of the geometry using signed distance functions. These functions give the shortest distance from any point in space to the boundary of the domain, with negative sign inside the region and positive sign outside [*Persson & Strang*, 2004]. Based on these, DistMesh first distributes a set of nodes interior to the computational domain. Then these interior nodes will be moved iteratively to obtain an equilibrium configuration, by minimizing the potential energy of the truss structure. In the last step, it will apply the terminate criterion when all nodes are fixed in space.

In order to resolve the coast geometry, small-scale physical processes and mediate steep-topography errors as well as guaranteeing computing efficiency, the regional model domain was divided into several polygons with different horizontal resolution (Fig. 2.5). The opening boundary regions were set with the lowest resolution of 4 km. Since we were most concerned about the tidal dynamics in Petermann Fjord and Nares Strait, horizontal resolutions for these two regions were set to 200 m and 500 m respectively.

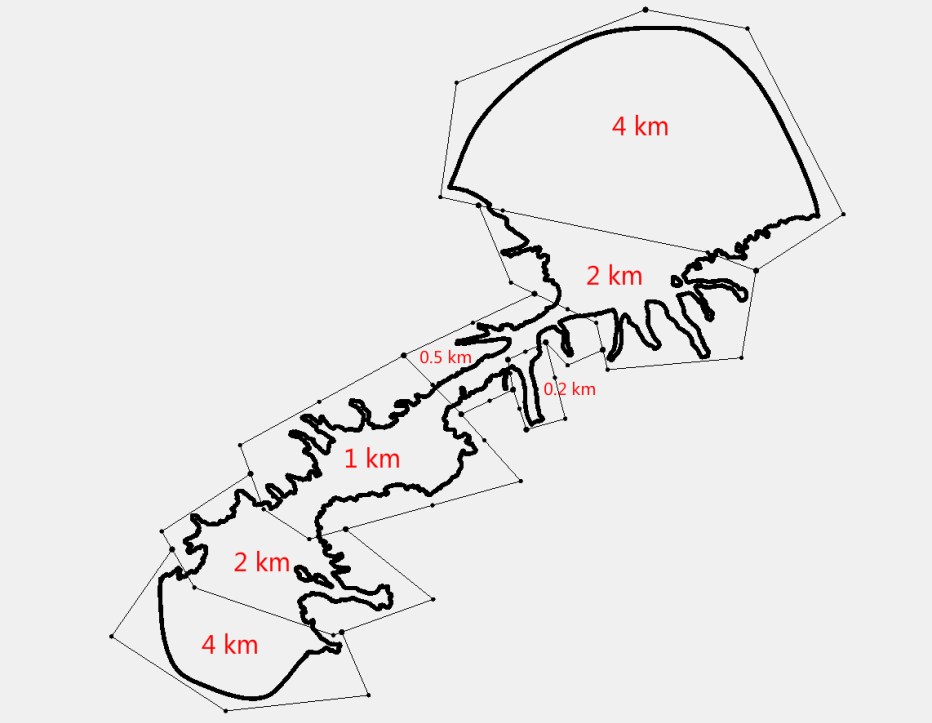

Figure 2.5: Resolution distribution (in polygons) for the computational domain.

The coastline used here was extracted from Global Self-consistent, Hierarchical, High-resolution Geography (GSHHG) database (www.ngdc.noaa.gov/mgg/shorelines/gshhs.html). Since the original coastline has the Petermann Glacier's front in the wrong location, we manually superimposed it according to the ice draft geometry. After removing those islands that are too small or far away to be affected by tidal currents, the entire coastline points were smoothed and redistributed in an averaged interval of 200 meters. The final obtained mesh grid has 112709 nodes in total (Fig. 2.6) and 10 sigma layers in vertical.

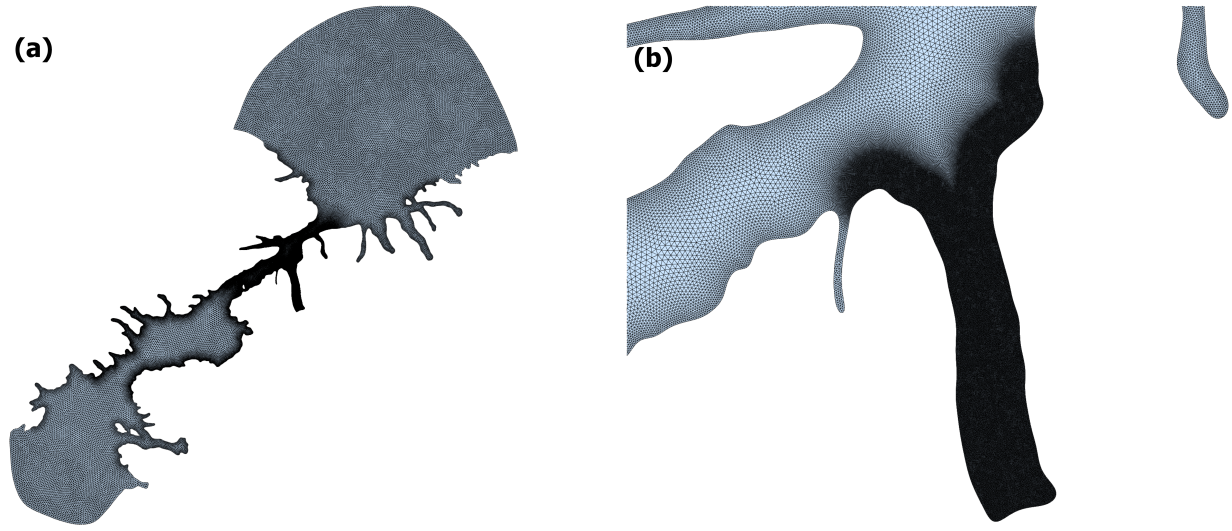

Figure 2.6: The computing triangular mesh grid.

(a) Entire model domain; (b) Petermann Fjord

2.2.2 Bathymetry smoothing

In the σ-coordinate system, insufficient bathymetric smoothing will produce noisy currents and exaggerated vertical mixing of temperature and salinity in areas of steep topography. If e and e′ are two adjacent cells of bathymetry h, then a simplified hydrostatic inconsistency can be expressed as:

$$rx_0(h; e, e') = \frac{|h(e)-h(e')|}{h(e)+h(e')} \tag{2-12}$$

The maximum of $rx_0(h;\ e, e')$ over any two adjacent cells is the slope factor $rx_0(h)$, and a particular choice of $rx_0(h) < 0.2$ results in relatively accurate representations of bathymetry and inhibits excessive mixing [*Sikirić et al.*, 2009]. In order to create a bathymetry in which the steepness is consistent with the spatially varying resolution, the following algorithm has been developed:

To include as steep as possible topography and keep as close as possible to reality, it is useful to apply a different amount of smoothing as function of model resolution. The bathymetry is gridded and smoothed into three different resolutions, depending on the area we are focusing on: Petermann Fjord and its adjacent region are set alone with a 200-m resolution; the open boundary regions are set alone with a 4-km resolution; the rest is set with a 2-km resolution. Each bathymetry matrix has been smoothed with a mean filter over a self-defined rectangle, such that at the respective resolution (4 km, 2 km, 200 m) the slope factor is below the chosen limit. The resolution matrix was resampled the same size with corresponding bathymetry matrix. Then we calculated a weight coefficient **w** based on different resolutions, following the algorithm defined below:

(1) For 4-km resolution, the **w** for each grid of resolution matrix changes linearly from 1 to 0 if the resolution ranges from 4 km to 2 km, else the **w** is 0;
(2) For 2-km resolution, the **w** for each grid of resolution matrix changes linearly from 1 to 0 if the resolution ranges from 2 km to 4 km or 2 km to 200 m, else the **w** is 0;

(3) For 200-m resolution, the **w** for each grid of resolution matrix changes linearly from 1 to 0 if the resolution ranges from 200 m to 2 km, else the **w** is 0.

This results in three different bathymetry matrices, not only at different resolutions, but also with different steepness and levels of details that are consistent with the maximum slope factor. Then merge them together by multiplying each weight coefficient matrix with corresponding bathymetry matrix and adding them up. This yields a bathymetry of varying steepness that satisfies the slope factor criterion in low-resolution areas but not over-smoothes the slopes in high-resolution areas. The smoothed bathymetry (Fig. 2.7) using the method described above and its slope factor after being interpolated to the FVCOM grid nodes (Fig. 2.8) are shown below:

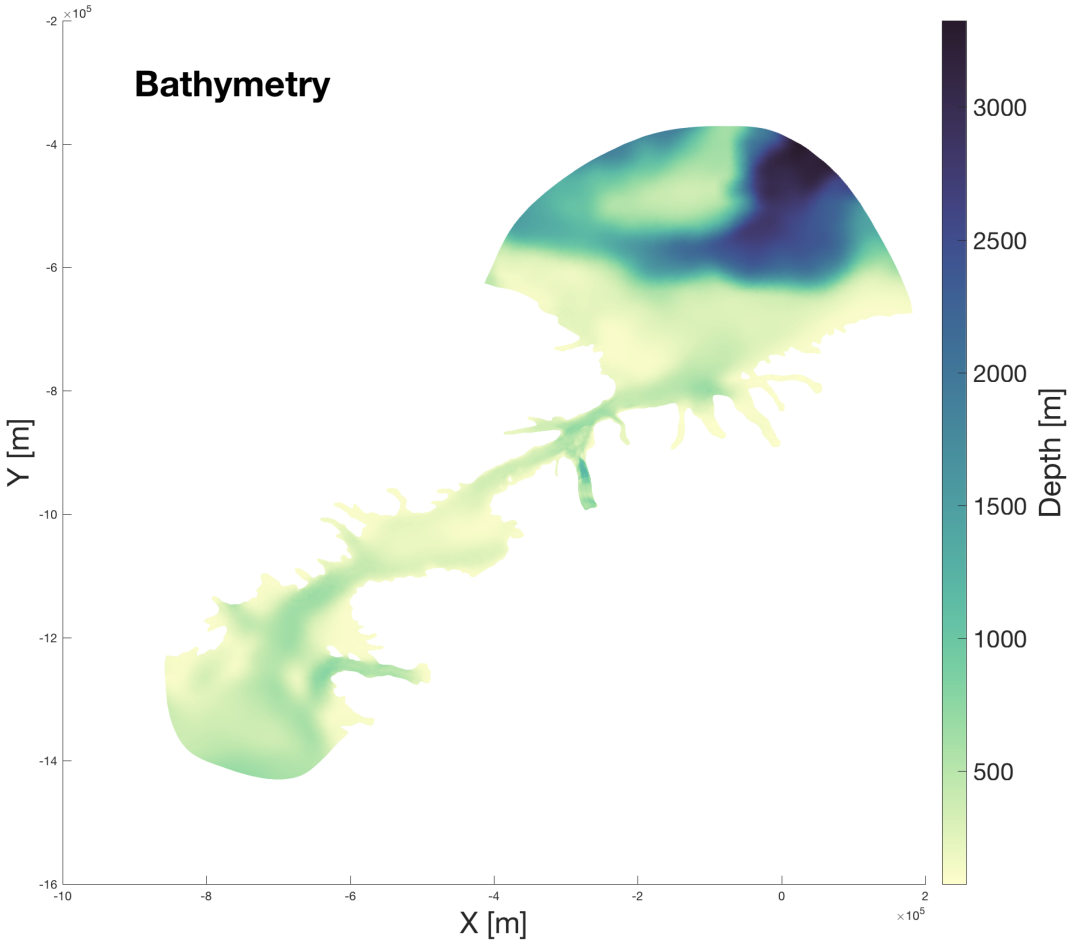

Figure 2.7: Smoothed bathymetry for the entire model domain.

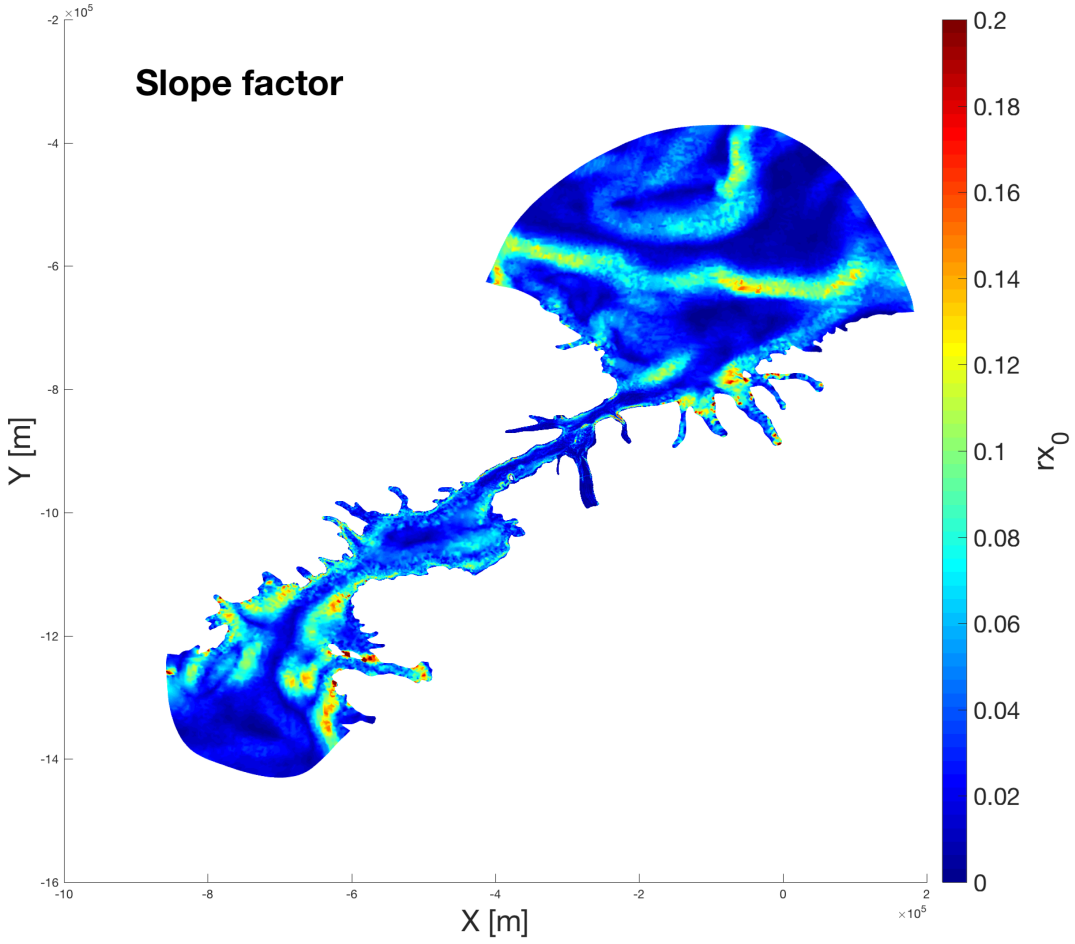

Figure 2.8: The distribution of slope factor in the entire model domain.

We see that after smoothing, the slope factor is controlled below 0.2 for almost the entire domain. The bathymetry in Nares Strait and Petermann Fjord exhibits a particularly good smoothing quality.

2.2.3 Boundary and initial setup

The physical forcing of the model is in the boundary conditions. The specified tides (Section 2.1.2) at the open boundaries are ramped to their full values at the beginning of simulation. Initial current velocities and water elevation are set to zero. The startup temperature and salinity are set as constants (-1.9°C and 33.8 psu). Aiming at simulating tides and tidal currents, affects from wind as well as heat and salt fluxes at the open boundaries are neglected. The simulation duration is from 1st June 2006 to 28th August 2006, with a calculation time step of 1 second and hourly outputs. In addition, a sponge layer is included, which can damp high frequency noise in the form of reflected waves generated in the model domain [*Chen et al.*, 2013].

3 Tide theory and tidal analysis

3.1 Theory of ocean tides

Causes of tides

Tides are periodic motion of the waters of the sea due to changes in the attractive forces of the Moon and Sun upon the rotating Earth. The rise and fall of tide is accompanied by horizontal movement of the water called tidal current. The principal tidal forces are generated by the Earth-Moon and Earth-Sun gravitational interactions. As these bodies rotate around their common centers of mass, a centrifugal force is generated that constrains them in their orbits, and prevents each from flying off in a straight line [*Segar*, 2012]. Then all points on and within the Earth will have the same centrifugal force, which is directed parallel to a line joining the center of the Earth and the center of the Moon or the Sun (Fig. 3.1).

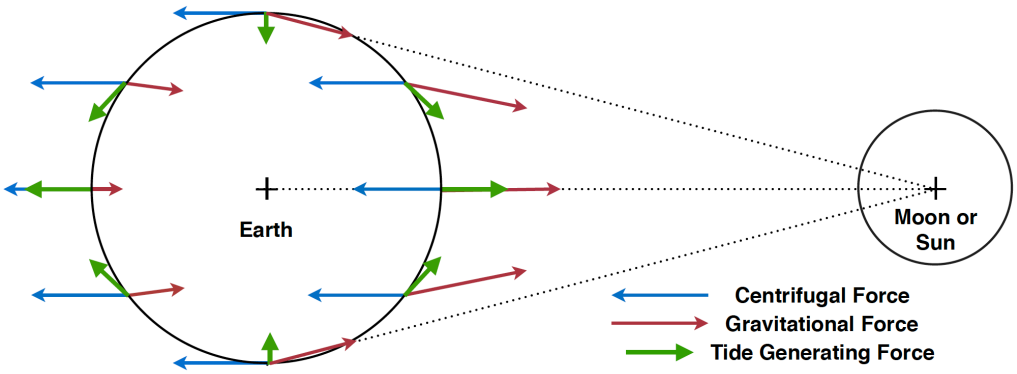

Figure 3.1: Schematic of the centrifugal force, the gravitational force and the tide-generating force. From [Davis, 2015].

The difference between the constant centrifugal force and the gravitational force at each point over the Earth's surface results in a residual force known as the tide-generating force. Newton's universal law of gravitation governs both the orbits of celestial bodies and the tide-generating forces that occur on them. The force of gravitational attraction between any two masses m_1 and m_2 is given by:

$$F = \frac{Gm_1m_2}{d^2} \tag{3-1}$$

where d is the distance between the two masses, and G is the universal gravitational constant. The main contribution to gravitational pull comes from the Moon. Due to its much greater distance away from the Earth, the Sun's effect is only 46 percent of the Moon's.

Tidal constituents

As the Earth-Moon and Earth-Sun systems rotate, the response to the tide-generating force at each point over the Earth's surface takes the shape of a sinusoid, resulting in the rising and falling of sea

levels and the waxing and waning of tidal currents. As the gravitational force is less on the side of the Earth facing away from the Moon or the Sun (Eq. 3-1), this force only cancels out a little part of the centrifugal force, hence a high tide forms both where the Earth is directly facing and facing away from the Moon or the Sun. This theoretically should result in two high tides per day and only two tidal constituents: the rotation of the Earth relative to the Moon (the M2 tidal constituent with a period of 12.42 hours) and the rotation of the Earth relative to the Sun (the S2 tidal constituent with a period of 12 hours).

In reality, however, the Earth, Moon and Sun's orbits are not circular and they do not orbit in the same plane. Hence there are hundreds of different tidal constituents, each with a distinct period, and the response at the Earth's surface to the tide-generating force represents the integrated effect of each of these tidal constituents. Among them many are too weak to have noticeable effect, and the ocean's response is often dominated by a combination of the eight major constituents listed in Table 3.1.

Tidal constituent	Name	Period (hrs)
Semi-Diurnal		
M2	Principal lunar	12.42
S2	Principal solar	12.00
N2	Lunar elliptic	12.66
K2	Lunisolar	11.97
Diurnal		
K1	Lunisolar	23.93
O1	Principal lunar	25.82
P1	Principal solar	24.07
Q1	Elliptic lunar	26.87

Table 3.1: Properties of the eight major tidal constituents.

3.2 Harmonic analysis

The tidal wave can be considered to consist of many constituents with smaller amplitudes and phases. Tidal amplitude varies depending on how the phases are synchronized with each other. The harmonic analysis aims at obtaining each constituent's amplitude and phase lag (called an epoch), which are referred to as harmonic constants. The amplitude is the maximum height that a tidal constituent contributes to the tide, and the epoch is the time when this maximum constituent contribution occurs (relative to a reference time, e.g. the Moon's transit over a local time meridian). The harmonic constants represent the contribution to the tide of the energy at each tidal frequency. By combining the amplitudes and epochs of all the tidal constituents, one can predict the tide at any time. In this thesis, the MATLAB package T_TIDE [*Pawlowicz et al.*, 2002] is used for tidal analysis and prediction. T_TIDE can perform classical harmonic analysis with nodal corrections, inference, and a variety of user-specified options. Predictions can also be made using the analyzed constituents.

The harmonic tide prediction equation

The formula for the height of one single tidal constituent h_1 at initial time can be written as

$$h_1 = fH\cos(V_0 + u - \kappa) \tag{3-1}$$

which is represented graphically in Figure 3.2. The amplitude is called H, which is often multiplied by a node factor f to include the modulation effect of the 18.6-yearly lunar nodal cycle [*Doodson*, 1921]. The expression $(V_0 + u)$ represents the theoretical phase of a constituent of the equilibrium tide (equilibrium argument), in which V_0 is a uniformly changing angular quantity involving multiples of the hour angle of the mean longitudes of the Moon and Sun, and the mean longitude of lunar or solar perigee. u is a slowly changing angle depending on the longitude of the Moon's node and varies over the 18.6-year lunar nodal cycle. The epoch κ is the angular retardation of the maximum of a tidal constituent of the observed tide behind the corresponding maximum of the same constituent of the theoretical equilibrium tide [*Parker*, 2007].

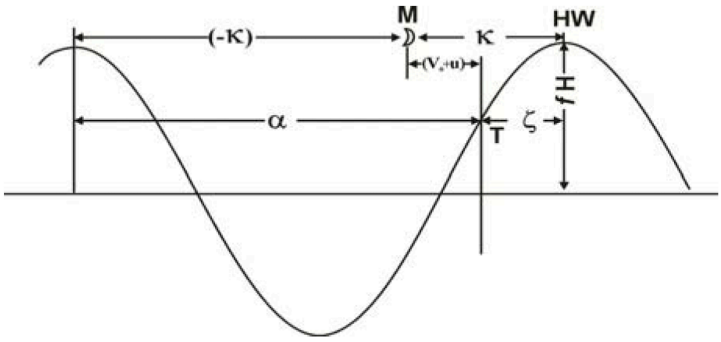

Figure 3.2: A graphical representation of the amplitude and epoch of a single tidal constituent and its time relationship to the Moon's transit. From [Parker, 2007].

T is a particular time of interest, M is the time when the constituent argument equals zero, so that the interval from M to the following high water (HW) is the epoch κ. The time interval from the previous HW to M is measured by the explement of κ (i.e., 360° –κ), which can be expressed as –κ.

It is the amplitude and the epoch that are calculated from a data time series using harmonic analysis. By summing up the contributions of the individual tidal constituents, the height of the tide at any time can be represented by the formula below from [*Schureman*, 1958] Schureman (1958):

$$h(t) = H_0 + \sum_{i=1}^{n} f_i H_i \cos(a_i t + \{V_0 + u\}_i - \kappa_i) \tag{3-2}$$

where n is the number of tidal constituents being used, a_i is the angular speed of tidal constituent i, $(a_i t + \{V_0 + u\}_i - \kappa_i)$ is the phase at any time t relative to the Moon's transit over the tide station. An entire predicted time series of tidal heights can be produced by using this equation. The tidal harmonic constants that come out of a harmonic analysis are the n pairs of amplitudes and epochs.

The harmonic tidal current prediction equations

The tidal current is a vector quantity usually given in terms of a speed and a direction. To harmonically analyze current data one must first transform each speed and direction pair into to orthogonal components. An option for the tidal current case is to treat the two orthogonal components together using complex algebra [*Pawlowicz et al.*, 2002]. In this case there is simply a single

prediction equation, since the current vector **v** is represented by the complex number $u + iv$ (where u, v are the orthogonal components of the tidal current). This complex prediction equation looks like

$$\mathbf{v}(t) = \mathbf{v}_0 + \sum_{i=1}^{n}\left(a_i^+ e^{i\sigma_i t} + a_i^- e^{-i\sigma_i t}\right) \tag{3-3}$$

where a_i represents the total contribution to the complex tidal vector **v** from constituent i, σ_i is the radian frequency of the constituent, and t is time. The complex coefficients a_i^+ and a_i^- multiply the complex exponential rotating elements ($e^{i\sigma_i t}$ and $e^{-i\sigma_i t}$), which represent the anticlockwise (positive) and clockwise (negative) rotary components respectively.

Least-squares-based harmonic analysis

For modern harmonic analysis, the least squares technique is the method most frequently used. This technique simultaneously solves for all harmonic constituents. The harmonic constants determined are those that minimize the sum of the square of the squared differences between the original data time series and the predicted time series. There are several advantages with this method over the less used Fourier series method: not restricted to continuous equally spaced data with no gaps; more flexibility on the length of the time series; one can determine how the variance between the data time series and the predicted time series from the calculated harmonic constants is reduced by each additional constituent included in the analysis [*Parker*, 2007].

Changing the tidal prediction equation to an equivalent form involving the sums of sines and cosines and including an additional term $h_r(t)$ to represent the residual time series, Eq. (3-2) becomes

$$h(t) = H_0 + \sum_{i=1}^{n} c_i \cos a_i t + \sum_{i=1}^{n} s_i \sin a_i t + h_r(t) \tag{3-4}$$

where

$$f_i H_i = \left(c_i^2 + s_i^2\right)^{\frac{1}{2}} \tag{3-5}$$

and

$$(V_0 + u) - \kappa_i' = -\tan^{-1}\frac{s_i}{c_i} \tag{3-6}$$

then the equation for each individual data point, the k^{th} data point is

$$h_k = H_0 + \sum_{i=1}^{n} c_i \cos a_i t_k + \sum_{i=1}^{n} s_i \sin a_i t_k + h_{r_k} \tag{3-7}$$

where k goes from 1 to *N*. The objective is to minimize the variance of the residual series e^2:

$$e^2 = \sum_{k=1}^{N} {h_r}_k^{\,2} = \sum_{k=1}^{N}\{h_k - \sum_{i=1}^{n}[c_i \cos a_i t_k + s_i \sin a_i t_k]\}^2 \tag{3-8}$$

Take partial derivatives of the residual Eq. (3-8) with respect to coefficients c_i and s_i, and set the results equal to zero, the minimum of e^2 can be found. Then 2n+1 simultaneous equations for n+1 tidal constituents will be produced, which are solved using matrix algebra.

4 Model results validation

The major objective of this chapter is to validate the capability of FVCOM in realistically reproducing the tides and tidal currents in Nares Strait. For this purpose, the first step is to examine the pressure gradient errors to ensure an acceptable level. The second step is to make comparisons between modeled results and observations.

4.1 Pressure Gradient Error (PGE) test

Internal pressure gradient estimation is problematic in FVCOM and other σ-coordinate ocean models. Artificial pressure gradients in these models may create artificial flow. Large errors in the estimates of internal pressure will yield wrong estimated geophysical flow, which is to a large extent determined by the balance between internal pressure and the Coriolis force [*Berntsen & Thiem*, 2007].

Under the assumption that the truncation error due to the σ-coordinate is negligible after bathymetry smoothing, there should be almost no current in the model domain without any forcing at open boundaries. The model is therefore integrated in a test mode for a 60-day running, with no tidal forcing introduced. The depth-averaged velocity induced by the pressure gradient error is plotted for day 30 (Fig. 4.1). The difference of velocity field between day 30 and day 60 is plotted in Figure 4.2.

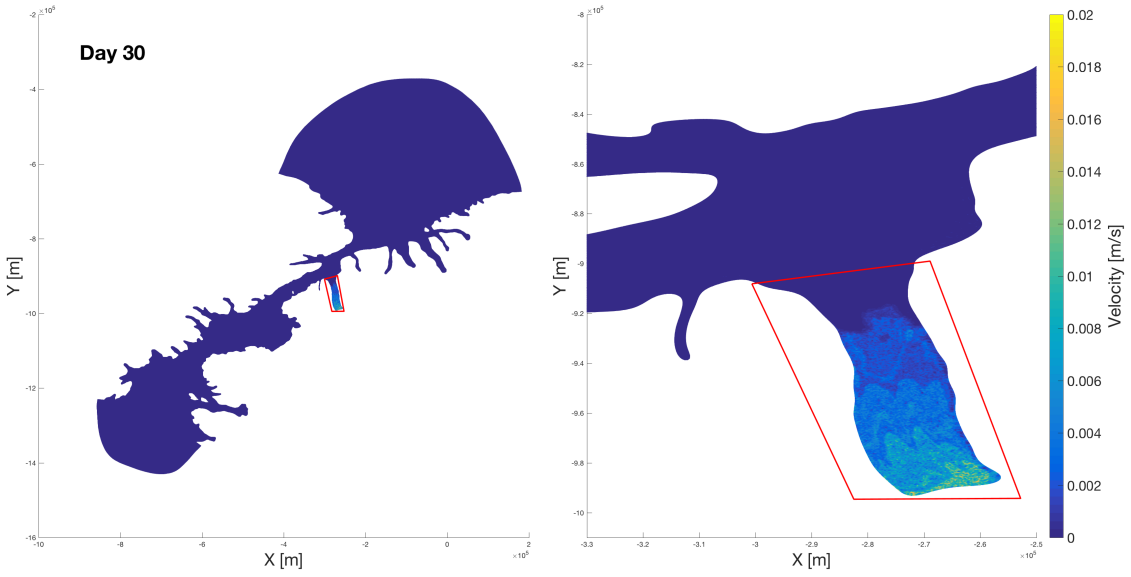

Figure 4.1: The distribution of the depth-averaged velocity induced by the pressure gradient error on day 30.

Left: Entire model domain; Right: Petermann Fjord

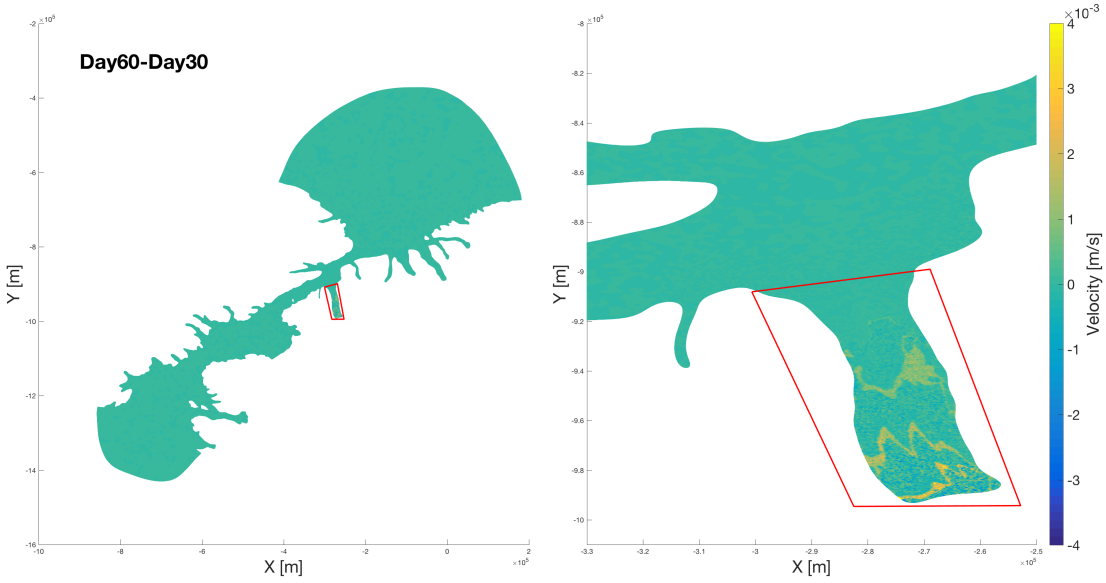

Figure 4.2: The distribution of the depth-averaged velocity difference day 60 and day 30.

Left: Entire model domain; Right: Petermann Fjord

After the model spinning up for 30 days, the error velocity field arrived at a statistically stable state, and with little variation for another 30 days. The velocity field did not change much for the entire model domain in the whole period. Even though the magnitude of velocity under Petermann Ice Shelf could reach a maximum of ~2 cm/s (particularly under the thickest ice), the error velocity was so small that could be ignored in the following tidal simulation.

4.2 Tides and tidal currents in Nares Strait

Nares Strait has been playing an important role in the interaction between Arctic and Atlantic oceans. Tidal dynamics dominate this area as the kinetic energy associated with tides is an order of magnitude greater than that associated the subtidal flow [*Davis*, 2015]. In order to study the role of tides in Nares Strait for water exchange with Petermann Fjord and validate the FVCOM simulation, the characteristic of tides and tidal currents in Nares Strait obtained from both observation and our model will be presented in this section.

Between the summers of 2003 and 2006, as part of the ASOF program, an array of ocean-sensing instruments was deployed at ~80.5°N to investigate the flux of seawater from the Arctic Ocean via Nares Strait [*Münchow & Melling*, 2008]. These instruments on sub-sea moorings were deployed across a 38-km wide cross-section of Kennedy Channel in August 2003, partly recovered in August 2006 [*Münchow & Melling*, 2008]. Each of these moorings carried a seabed-mounted Acoustic Doppler Current Profiler (ADCP), making measurements of the average current velocity from about 30 m below the surface to about 15 m above the seafloor (Fig. 4.3).

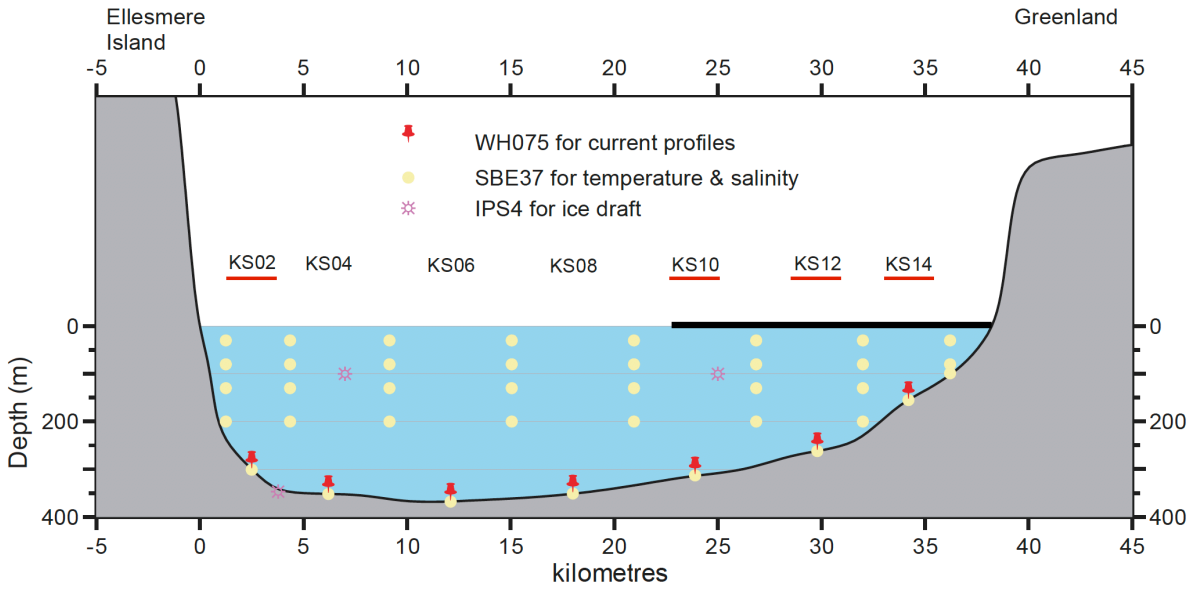

Figure 4.3: Locations of instruments on the moorings of the Kennedy Channel South (KS) section, the ADCPs are denoted by the red pins. From [Davis, 2015].

The ADCPs recorded data twice hourly, a pressure sensor in each ADCP provide a concurrent measurement of the pressure on the same time basis [*Davis*, 2015]. Unfortunately, the instruments in sites KS04, KS06 and KS08 were not recovered in 2006, leaving a wide gap without data. Hence this section focuses on the data returned by KS04 against Ellesmere Island, and KS10, KS12 and KS14 against Greenland. The four recovered ADCPs on the section delivered a full three-year data record. Table 4.1 summarizes the data obtained from them, full details for all the moorings can be seen in [*Münchow & Melling*, 2008].

Name	Longitude, W	Latitude, N	Depth, m	Distance, km	Record, days
KS02	68.8744	80.5538	302	2.2	1103
KS10	67.9296	80.4388	299	23.9	1105
KS12	67.6709	80.4092	263	29.6	1104
KS14	67.4458	80.3884	157	34.4	1103

Table 4.1: Mooring locations and records.

4.2.1 Tides in Nares Strait

The tides in Nares Strait are forced by sea-level differences at tidal frequencies between its northern and southern ends. The sea-level differences arise from differences in the phase and amplitude between the tidal wave propagating counter-clockwise around the Arctic Ocean to the northern end of Nares Strait and that propagating counter-clockwise around Baffin Bay [*Padman & Erofeeva*, 2004]. Both of the tidal waves originate from the North Atlantic.

Based on the three-year observational records in the ASOF experiment, it was found that the tidal flow in Nares Strait was dominated by seven major tidal constituents: M2, K1, S2, O1, N2, P1 and K2 [*Münchow & Melling*, 2008]. The most significant tidal constituent M2 contains between 55~57% of the total tidal energy, followed by the K1 and S2 tidal constituents corresponding to between 19~21% and 9~10% respectively [*Münchow & Melling*, 2008]. Overall the semidiurnal tides dominate in Nares Strait.

The estimate of tidal sea-level oscillations at the mooring locations comes from predictions by the barotropic model AOTIM, which agrees extremely well with observations in Nares Strait if adequate bottom topography is acquired [*Padman & Erofeeva*, 2004]. The harmonic constants of four major tidal constituents (M2, S2, K1, O1) using T_TIDE are summarized in Table 4.2.

Tidal constituents	**Amplitudes (meter)** (KS02 KS10 KS12 KS14)				**Phases (degree)** (KS02 KS10 KS12 KS14)			
M2	1.0361	1.0386	1.0354	1.0364	109.60	113.01	113.98	115.03
S2	0.4194	0.4203	0.4194	0.4199	159.31	162.49	163.31	164.18
K1	0.2554	0.2747	0.2797	0.2859	279.64	288.23	290.84	293.35
O1	0.0806	0.0933	0.0966	0.1002	224.83	236.79	240.21	243.50

Table 4.2: The amplitudes and phases of four major tidal constituents at the mooring locations.

Model results show that M2, S2 and K1 are still the dominant tidal constituents in the model results, but the S2 tidal constituent is more significant than K1. In fact, it is the existence of a thick shear layer, or the difference in gradient of the tidal semi-major-axis amplitude change over depth that makes the amplitude of the S2 tidal constituent smaller than that of the K1 in a depth-averaged sense [*Davis*, 2015].

In order to assess the representation of tidal propagation from FVCOM (the AOTIM specifically), Figure 4.4~4.6 show the amplitude and phase of the M2, S2 and K1 tidal constituents. The results are obtained by conducting a T_TIDE harmonic analysis for the surface elevation output at all nodes during the last one month of simulation.

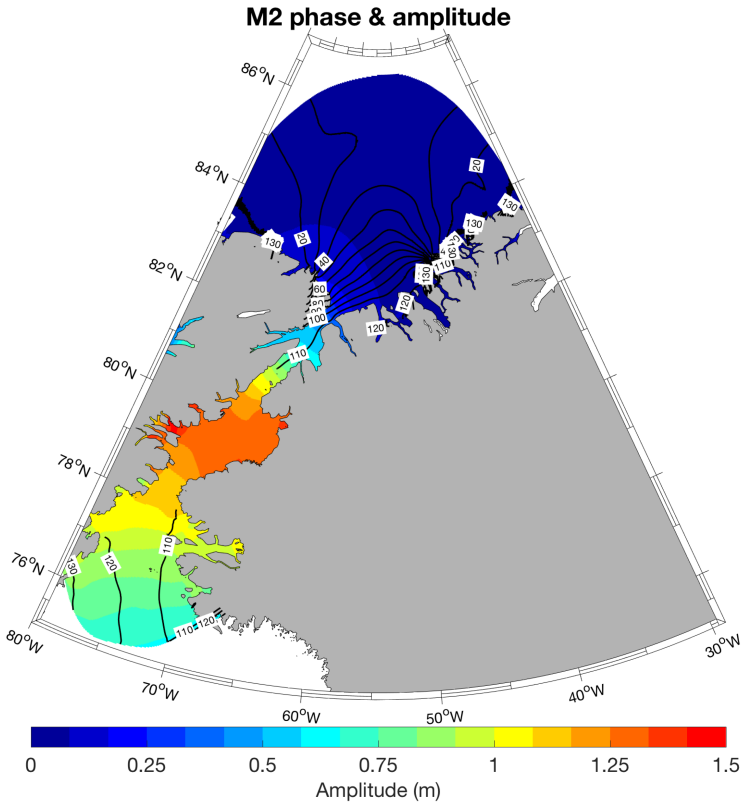

Figure 4.4: Amplitude and phase of the M2 tidal constituent in Nares Strait from FVCOM.

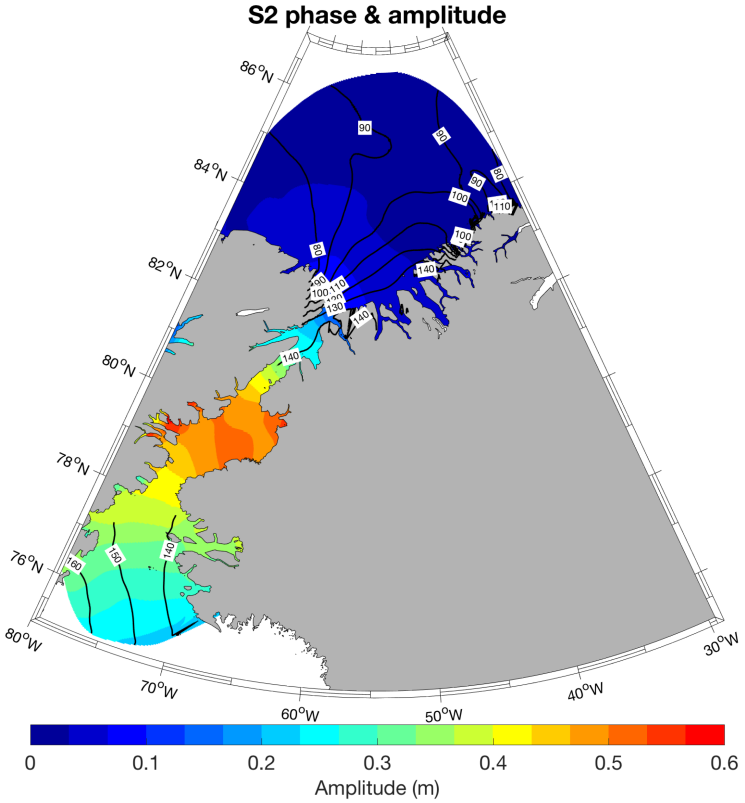

Figure 4.5: Amplitude and phase of the S2 tidal constituent in Nares Strait from FVCOM.

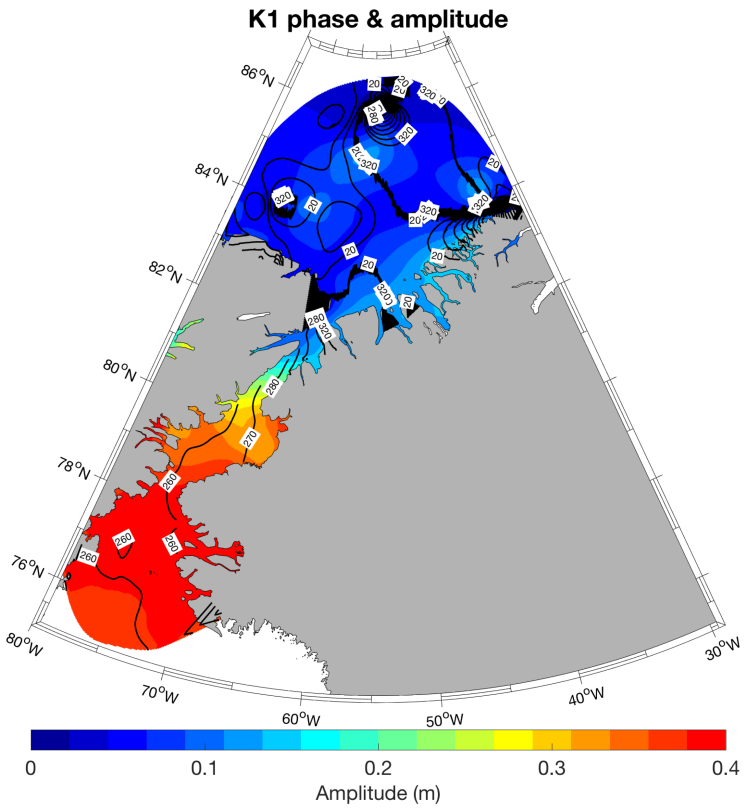

Figure 4.6: Amplitude and phase of the K1 tidal constituent in Nares Strait from FVCOM.

The phase lines in Figure 4.4 and Figure 4.5 show that the phase of the M2 and S2 tidal waves as they enter Nares Strait are ~110° and ~140° respectively. An amplification of the M2 and K2 tides also occurs in the middle of the strait. In contrast, the phase of the K1 constituent consistently increases with latitude (Fig. 4.6), but there is an enhancement of the K1 amplitude (0.3~0.4 m) to the south of Nares Strait. The results for tides of the FVCOM are consistent with those of *Davis*' work [2015]. According to his conclusion, the M2 and S2 tidal constituents exhibit a characteristic of the standing wave (thus explaining the unusually strong tidal currents in this region), while the tidal wave associated with the K1 tidal constituent has neither purely progressive nor purely standing wave characteristics.

4.2.2 Tidal currents in Nares Strait

The two counter-rotating circular velocity vectors of each tidal constituent determines that they trace an ellipse path over one period. The ellipse parameters for each constituent consist of the semi-major axis, the semi-minor axis, the orientation and the phase [*Parker*, 2007]. Given that the two components are rotating at the same frequency but in opposite directions, the semi-major (minor) axis can be interpreted as the magnitude of the tidal current at the point in time when the two rotary vectors are aligned (opposed). The orientation of the ellipse is defined as the angle between the positive u axis and the semi-major axis that points in the direction of the positive v axis [*Davis*, 2015]. To further validate the modeled results, we made a comparison between the ellipse parameters from FVCOM and that from observation for different tidal constituents at four mooring locations (Fig. 4.7).

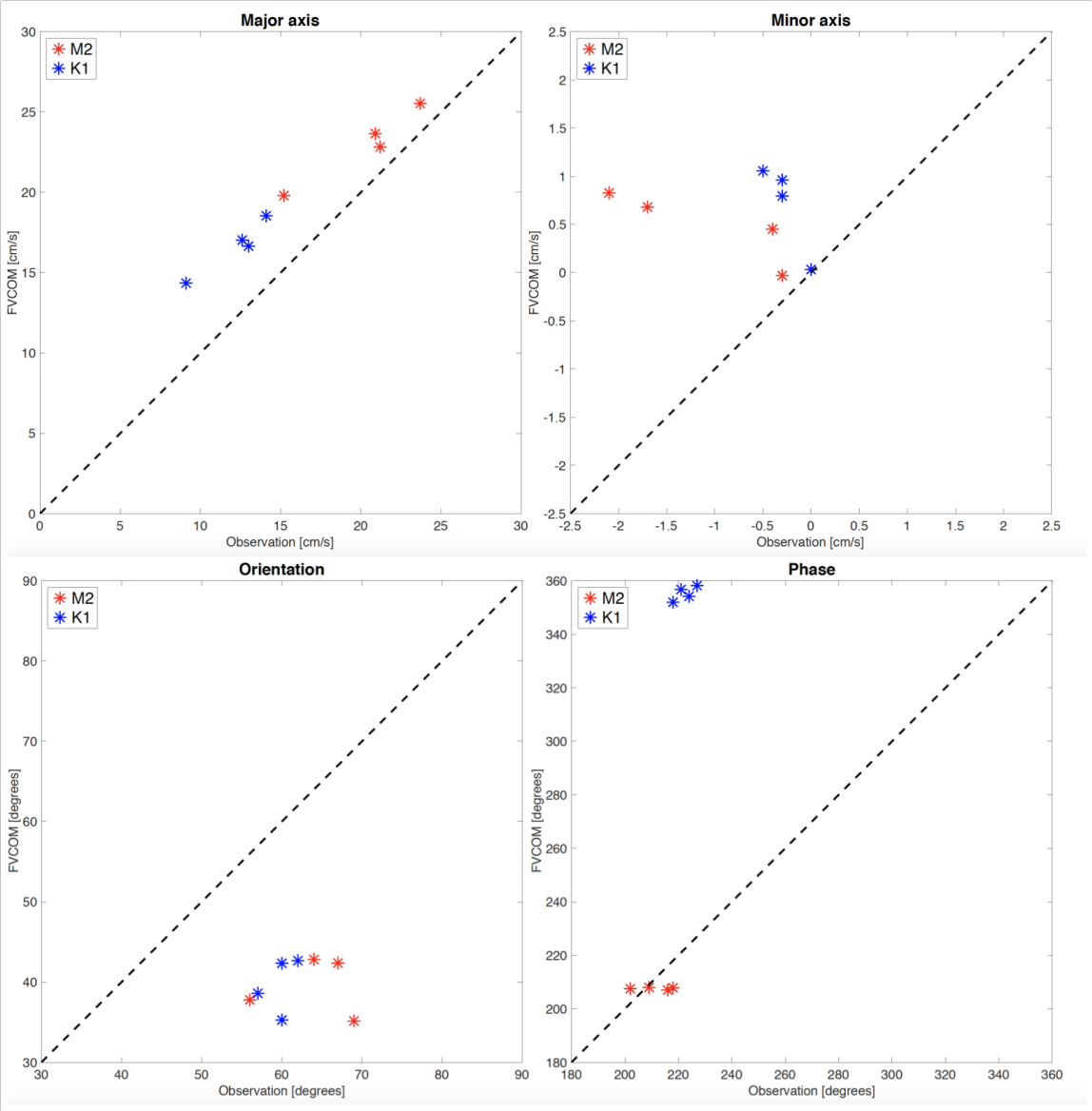

Figure 4.7: M2 and K1 tidal ellipse parameters at the mooring locations from FVCOM and observation.

The ellipse parameters were also estimated by the T_TIDE harmonic analysis and we only chose the M2 and K1 tidal constituents due to limited observations obtained from [*Münchow & Melling*, 2008]. The correlation between model results and observation shows that except for the phase of K1 tidal constituent, most of the other parameters at different locations are consistent with each other.

The phase difference between the maximum velocity and the maximum sea surface height at any given point is different for a progressive wave and a standing wave (0° and 90° respectively) [*Segar*, 2012]. Therefore, the nature of the tidal wave associated with each of the major tidal constituents can be determined by comparing the phase of the sea-level oscillation to that of the depth-averaged along-strait tidal velocity (Fig. 4.8), observational information is provided in [*Davis*, 2015].

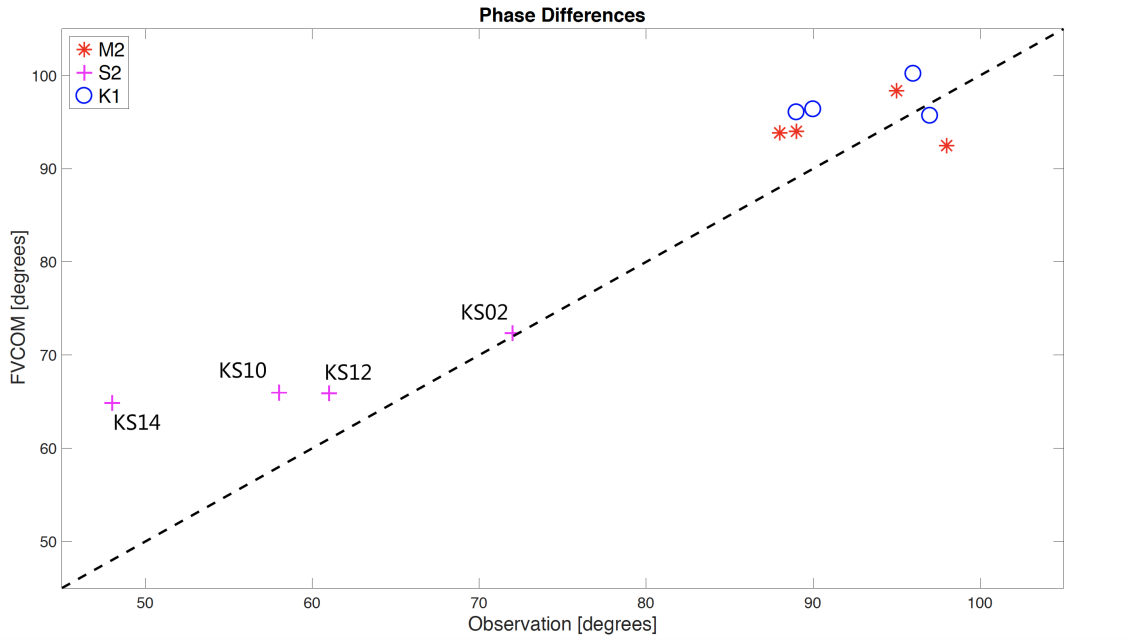

Figure 4.8: Phase differences between tides and tidal currents at the mooring locations from FVCOM and observation.

The model results agree quite well with observations. For the M2 and S2 tidal constituents, the phase difference is close to 90° at all mooring locations. For the K1 tidal constituent, however, the phase difference is approximately 60° at the center of the strait (KS10 and KS12), increasing to ~72° at KS02 and decreasing at KS14. These suggest that the characteristics of the tidal waves associated with the M2, S2 and K1 tidal constituents are consistent with those indicated in the previous Section 4.2.1.

Above all, the tidal forcing with AOTIM at the southern and northern open boundaries is sufficient to impose the correct tidal forcing on the model, although main uncertainties remain because of inadequate bottom topography in the region of focus, Petermann Fjord.

5 Water exchange under tidal currents

The water exchange in estuaries and fjords is usually driven by complex Lagrangian physics. This means that the tidally-averaged movements of water parcels in a fjord are not driven by residual current vectors that are estimated by averaging tidal currents at fixed locations. One must trace the movement of individual fluid particles to properly estimate water exchange and movement in a fjord. For this reason, we conducted 2-D Lagrangian particle tracking experiments to examine the nature of the water exchange in Petermann Fjord and its adjacent strait area.

5.1 General background and preparation

5.1.1 Residual current

The residual current is commonly defined as the tidal-cycle average of tidal current. With inclusion of multi-periods of the eight major tidal constituents (M2、S2、N2、K2、K1、O1、P1、Q1) during the two-month simulation, the residual current described here is the output monthly mean flow that exists in the strait and the fjord. The averaged velocity field for the last simulation month is shown in Figure 5.1, in which the Petermann Fjord region is included inside a polygon. The ice-shelf region is also outlined by a polygon, whose north side follows along the edge of Petermann Ice Shelf (Fig. 5.2).

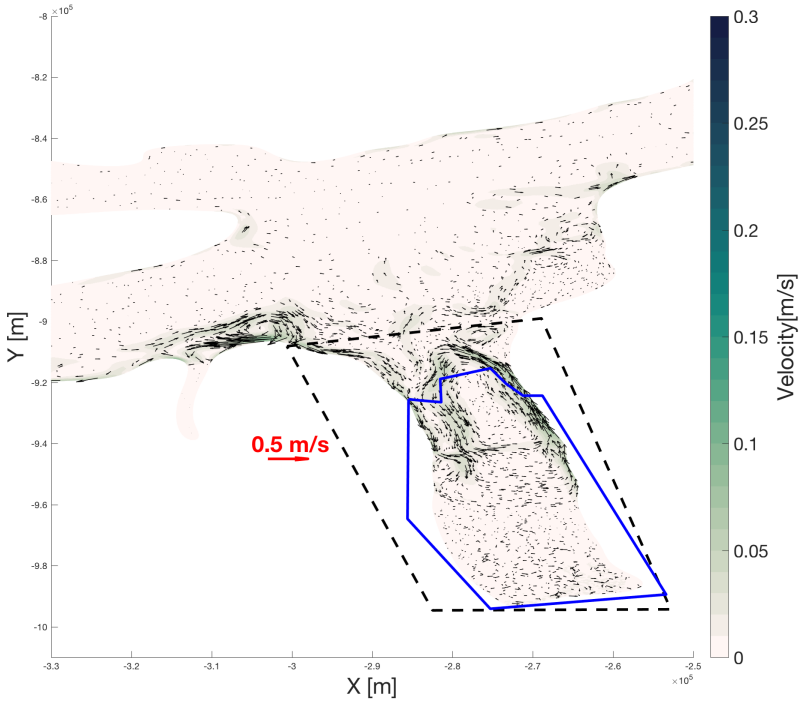

Figure 5.1: Distribution of the model-predicted residual currents in Petermann Fjord and adjacent Nares Strait. Petermann Fjord region (dashed black polygon); Ice-shelf region (blue polygon)

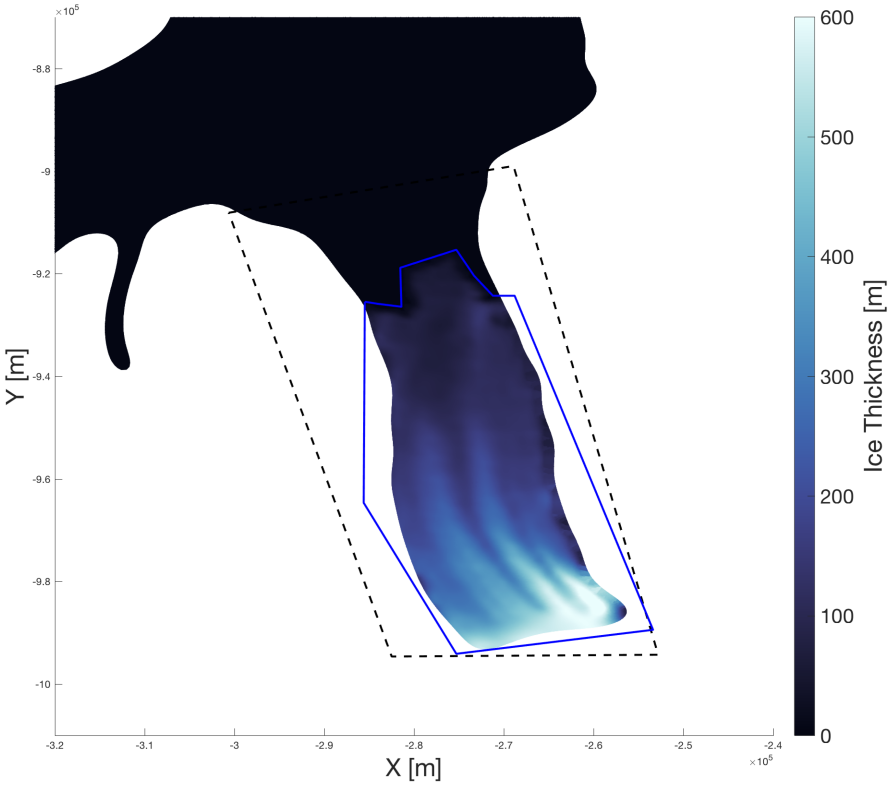

Figure 5.2: The ice thickness of Petermann Ice Shelf.

Petermann Fjord region (dashed black polygon); Ice-shelf region (blue polygon)

Outside Petermann Fjord, there is a general south-to-north flow in Nares Strait. It has a mean velocity of about 0.15 m/s, stronger in south than in north. The flow from southern Nares Strait bifurcates into three branches at the northwest of the fjord mouth, one forms a small anticyclone and move back to south, one enters the fjord and reaches below the ice shelf, the other passes the fjord mouth and move farther north. Within the fjord mouth, a cyclonic gyre is significant, which is consistent with satellite observation [*Johnson et al.*, 2011]. The cyclonic circulation causes water exchanges at the fjord mouth, with a magnitude of around 0.2 m/s. Seawater that flows into the fjord mouth can be transported to beneath the floating ice shelf and cause basal melting.

5.1.2 Particle seeding

In order to represent water exchange properties beneath Petermann Ice Shelf and in adjacent Nares Strait, Lagrangian particles were seeded at three cross-sections: Ice-shelf (I) section locates near to the northern boundary of the ice-shelf polygon; North (N) and South (S) sections locate at the northeast and northwest of the fjord polygon respectively (Fig. 5.3). Each of these sections consists of 50 points along the straight line. Corresponding to the last tidal simulation month, one particle is released at each of the section points every hour and all particles share a 30-day lifecycle.

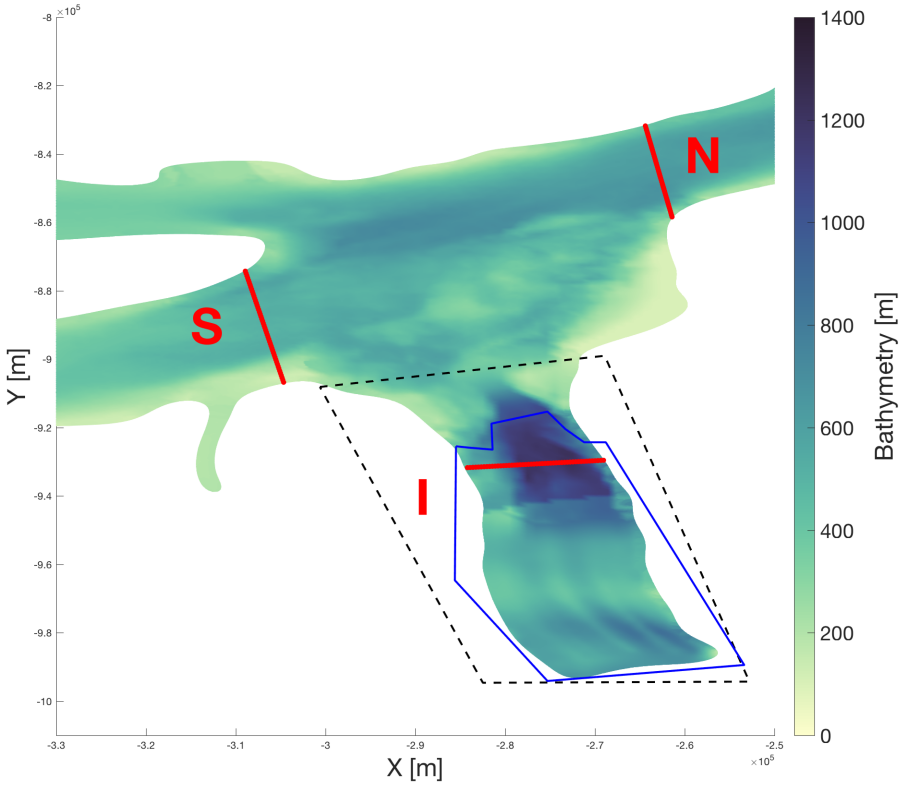

Figure 5.3: Locations of the particle seeding sections (in red lines).

N: North section; S: South section; I: Ice-shelf section

5.2 Lagrangian particle tracking

5.2.1 Passive particle trajectories

In the passive particle simulations, the particles followed the path of the fluid without vertical motion. The distribution of the particles initially seeded at the sections and their age are exhibited in Figure 5.4~5.6. Here the 'age' refers to the duration of each particle's existence and it shall not exceed 30 days. All the data are the averaged value recorded in 100 m × 100 m bins.

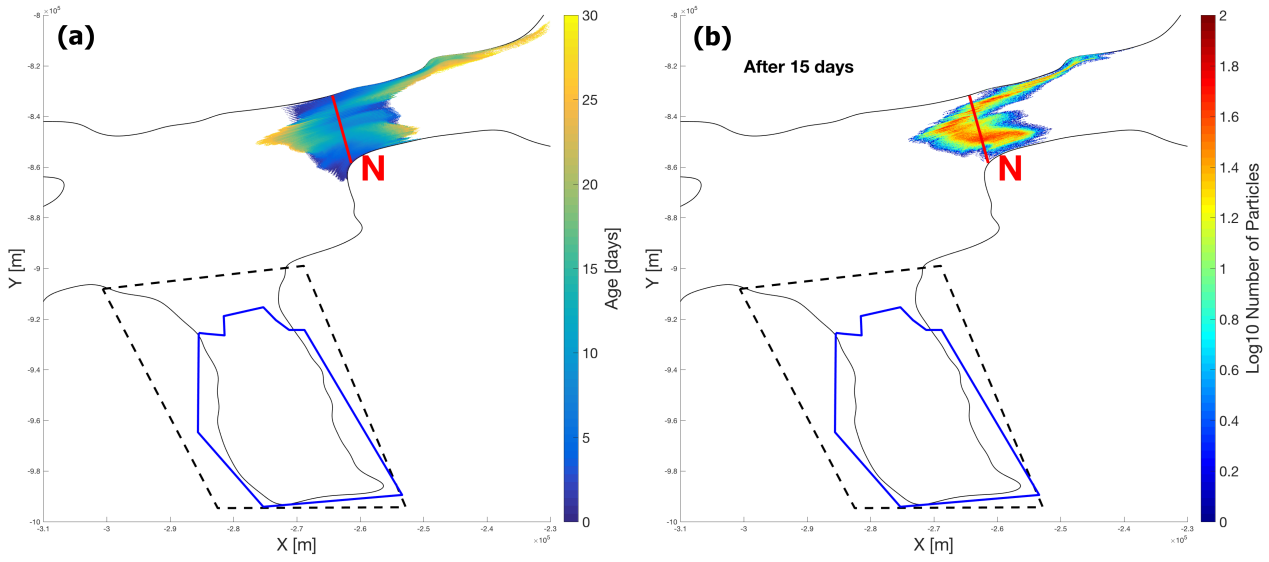

Figure 5.4: Trajectories and fates of particles seeded at the North section.

(a): Age distribution of all particles; (b): Amount distribution of particles with age of 15 days

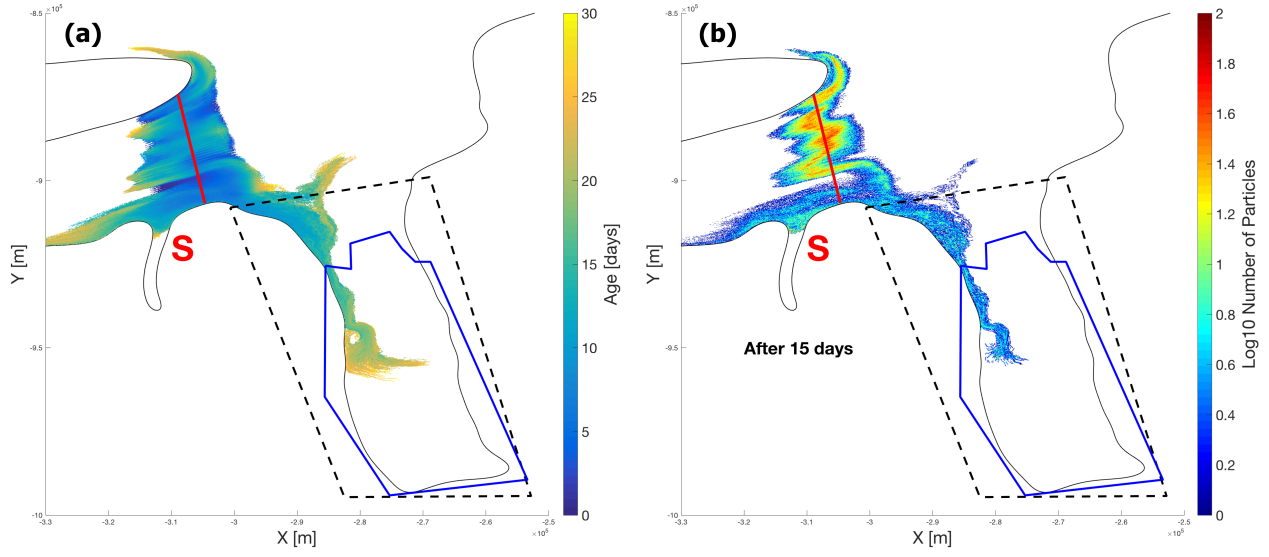

Figure 5.5: Trajectories and fates of particles seeded at the South section.

(a): Age distribution of all particles; (b): Amount distribution of particles with age of 15 days

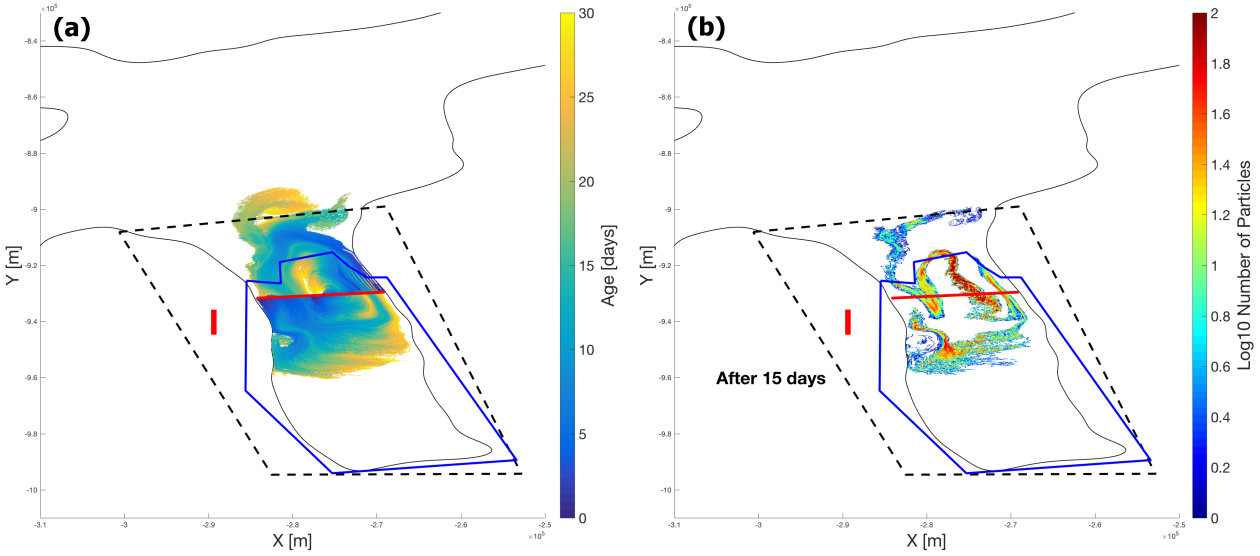

Figure 5.6: Trajectories and fates of particles seeded at the Ice-shelf section.

(a): Age distribution of all particles; (b): Amount distribution of particles with age of 15 days

Trajectories of the passive particles seeded in transport simulations followed the pattern of tidal residual currents in Nares Strait and Petermann Fjord. Particles at both the N Section and the S Section exhibited an along-strait reciprocation motion (Fig. 5.4~5.5), indicating the periodical tidal current flow. At the N Section, except for particles at the northern end (against the Ellesmere Island) that can move further north, most particles reached to a short distance (~10 km) away from the section. The process can be almost completed within 15 days, when particles primarily concentrated close to the section. At the S Section, there was also a bifurcation at the northwest side of the fjord region, which is consistent with the residual current flow shown in Figure 5.1. Even though a large amount still concentrated across the section in short ranges after 15 days, particles were able to enter the fjord and even expand into the ice-shelf region. As for particles seeded at the I Section (Fig. 5.6), they followed the cyclonic path at the fjord mouth. The irregular distribution of the 15-day-old particles outlined the cyclonic gyre as well.

5.2.2 Transport and retention of particles

Trajectories of particles, seeded at the S Section and the I Section in particular, demonstrated two major pathways of water transported to the ice shelf: one from the southern part of Nares Strait, the other from the northern part of Nares Strait. They are probably important sources of oceanic heat transport, which can cause basal melting of Petermann Glacier. To quantify the possible effects from tidal currents, the concentration of particles (seeded at the S Section) transported into the fjord region and the ice-shelf region with different ages are calculated respectively at first (Fig. 5.7).

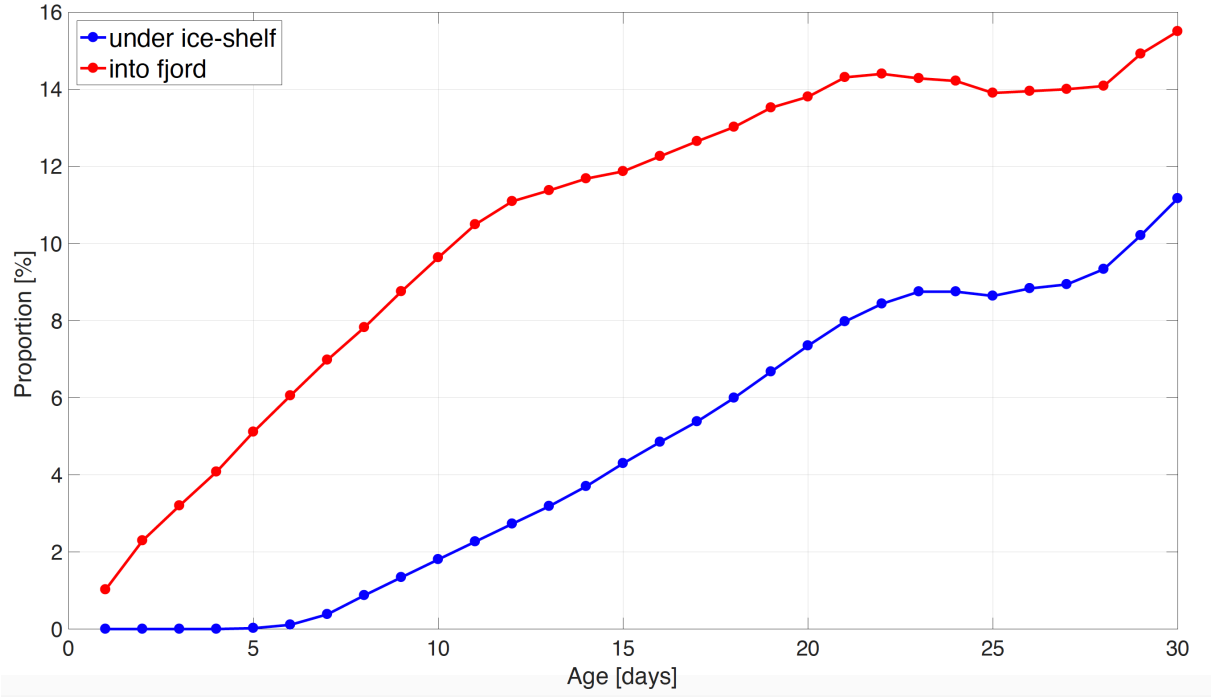

Figure 5.7: The proportion of particles transported from the S Section into the fjord and under the ice shelf.

As shown in the previous section, for particles released in Nares Strait, only those seeded at the S Section could reach into Petermann Fjord and the ice-shelf region during the 30-day experiment. Although in a quite small amount (~1%), particles could be transported into the fjord within only one day. After being seeded for 5 days, some particles started to arrive beneath the ice shelf. With longer age, the percentage of corresponding-age particles that entered the two regions kept increasing. After 20 days, most of these particles within the fjord have arrived below Petermann Glacier. In addition, the proportions of the 30-day-old particles transported into the fjord and the ice-shelf region were approximately 16% and 11% respectively, indicating potentially considerable water and heat transport.

To quantify the retention of particles below the ice shelf, the residual time of all particles staying within the ice-shelf polygon after they were initially released at the I Section was estimated and classified (Fig. 5.8).

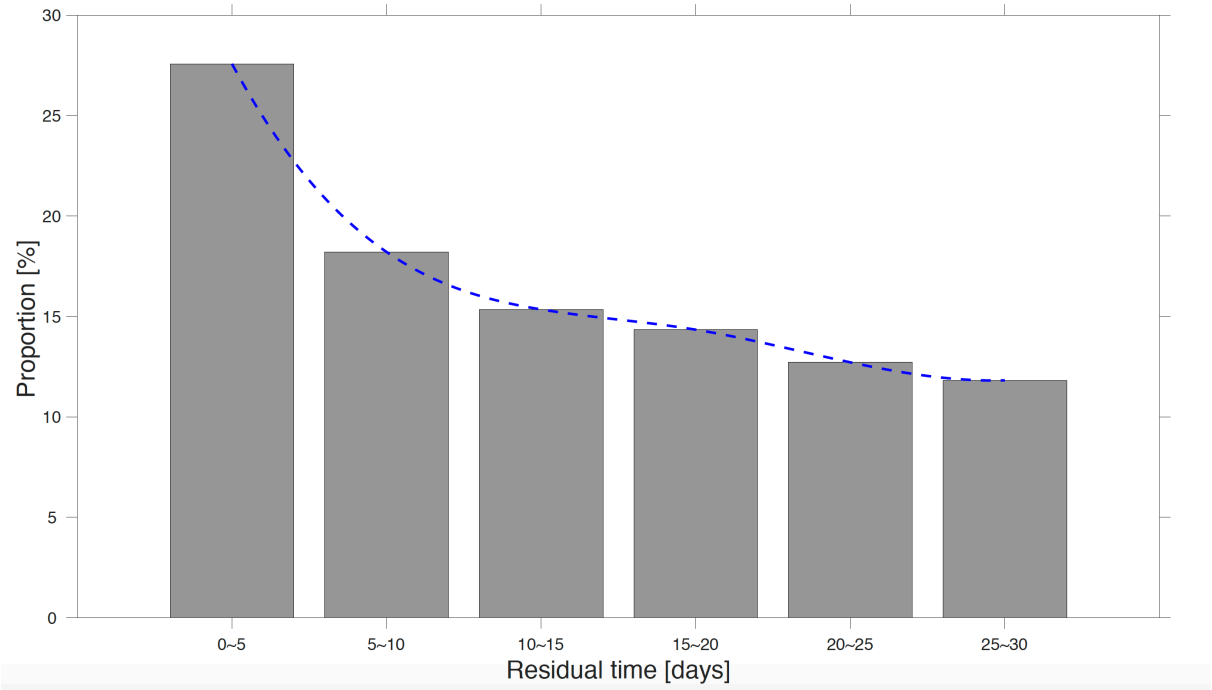

Figure 5.8: The distribution of below-ice-shelf particles with different residual time.

Mean variation trend is displayed in dashed blue line

All particles seeded at the I Section were initially below the ice shelf. Most of them stayed inside the ice-shelf region within 10 days, adding up to about 45%. The older the particles were, the larger proportion of them got transported outside the ice-shelf region under the cyclonic gyre. Only about 12% of particles retained after they had been moving for more than 25 days. Following the tidal residual currents, seawater below the northern font of Petemann Ice Shelf can be transported outward even to Nares Strait (Fig. 5.6). However, the amount of the water transported and corresponding timescale may vary with different locations. The statistics of particle residual time are calculated from all points of one single seeding section, further investigation is required for quantifying the water exchange under the ice shelf.

6 Conclusion

The floating ice shelf of Peterman Glacier, one of four major outlet glaciers in Greenland, interacts directly with the ocean. Basal melting is confirmed by in-situ surveys to be the dominant component of the mass balance of Petermann Ice Shelf, illustrating that ice-ocean interactions may exert a dominant control on the evolution of ice shelves in Greenland [*Rignot & Steffen*, 2008]. New insights for the tides in Nares Strait and Petermann Fjord are provided in this study by numerical modeling based on the FVCOM.

In a two-dimensional setup, the FVCOM is validated by conducting a PGE experiment. The depth-averaged velocity field obtained from the 60-day test case reached a stable state after 30 days. There was little variation for the entire modeling domain for the rest 30 days. Despite that the maximum of the error velocity was about 2 cm/s only at the thickest ice-shelf area, it was small enough to be ignored as the truncation error caused by approximations in the σ-coordinate system.

The output from the FVCOM was verified by comparing with the in-situ measured tidal currents in Nares Strait. It was shown that the M2, S2 and K1 tidal constituents dominated the strait. Among them the semi-diurnal tides M2 and S2 propagated through the strait with standing wave characteristics. The diurnal tide K1 exhibited a mixed feature between standing wave and progressive wave. Harmonic analysis of the three major tidal constituents also showed that the FVCOM results agreed well with observations. Most ellipse parameters of the M2 and K1 tidal constituents at all mooring locations of the model were consistent with those of observation, apart from the discrepancy with the phase of K1. The differences between phases of tides and those of tidal currents from the model and observation were consistent with each other as well.

In addition, tidal residual currents generally flowed from south to north in Nares Strait, with a mean velocity of about 0.15 m/s, but weakened to north. The flow from south bifurcated into three branches at the northwest of the Petermann Fjord mouth, one formed a small anticyclone and move back to south, one entered the fjord and reached below the ice shelf, the other passed the fjord mouth and moved farther north. A significant cyclonic gyre was observed at the fjord mouth. With an average magnitude of about 0.2 m/s, it may serve as an important driving force for water exchange under the ice shelf.

Passive Lagrangian particles were released in Nares Strait and below Petermann Ice Shelf to investigate water exchanges between the strait and the fjord as well as between the fjord and the ice-shelf bottom. Particle trajectories in a 30-day duration followed the general circulation of residual currents. It was shown that there were two major pathways at the north and northwest sides of the fjord mouth for water transport to beneath the ice shelf. One of the pathways originated from southern Nares Strait, particles against Greenland could travel to the ice shelf after 5 days. With enough time, the proportion of these particles increased with their ages, indicating a possible large amount of oceanic heat transport. The other pathway originated from northern Nares Strait, following the cyclonic flow within the fjord. It could serve as a heat supply from the North Atlantic, contributing to ice-shelf bottom melting. Taking the whole one particle seeding section into account, most of the particles retained beneath the ice shelf within half a month. More and more particles would be

transported outside the ice-shelf region eventually as their ages increased. Similarly, the durations of water and heat transport beneath ice also depend on their initial locations and other conditions.

6.1 Future work

The results so far present the ice-shelf-ocean interaction at Petermann Glacier under tidal currents. Physics of tidal propagation in Nares Strait should be further understood. Lagrangian particle tracking experiment can be put further to better represent and quantify the water exchange in Petermann Fjord. For example, more seeding sections at different locations can be set up.

The task of improving model predictability need to be highlighted. The model should be able to accurately represent all those tightly coupled components in the system both at small length scales and short timescales. Implementing three-dimensional equations, and thus including salinity and temperature should improve the results. The unknown bedrock topography in Petermann Fjord and beneath Petermann Ice Shelf has limited the authenticity of simulations, so improved knowledge of the bathymetry should be the next target. Accordingly, the grid resolution can be improved as well. These all together will be a good start for future investigation of the mechanism of oceanic heat transport towards the floating ice shelf, considering ocean circulation and environmental factors such as atmospheric forcing and sea ice.

Comparing FVCOM results with more other observations and modeled results is also a good way to verify the model. Observations in our focused regions have been limited so far, hence with more comparisons the accuracy of FVCOM simulations and the understanding for ice-ocean dynamics will be enhanced.

References

Bamber, J. L., Siegert, M. J., Griggs, J. A., Marshall, S. J., & Spada, G. (2013). Paleofluvial mega-canyon beneath the central Greenland ice sheet. *Science*, **341**(6149), 997-999.

Berntsen, J., & Thiem, Ø. (2007). Estimating the internal pressure gradient errors in a σ-coordinate ocean model for the Nordic Seas. *Ocean Dynamics*, **57**(4), 417-429.

Chen, C., Beardsley, R. C., & Cowles, G. (2013). An unstructured grid, finite-volume coastal ocean model: FVCOM user manual. *SMAST/UMASSD*, 6-8.

Chen, C., Liu, H., & Beardsley, R. C. (2003). An unstructured grid, finite-volume, three-dimensional, primitive equations ocean model: application to coastal ocean and estuaries. *Journal of atmospheric and oceanic technology*, **20**(1), 159-186.

Davis, P. E. D. (2015). *The dynamics of a changing Arctic Ocean.* (D. Phil.), University of Oxford, Oxford, UK.

Doodson, A. T. (1921). The harmonic development of the tide-generating potential. *Proceedings of the Royal Society of London. Series A, Containing Papers of a Mathematical and Physical Character*, **100**(704), 305-329.

Gladish, C. V., Holland, D. M., Holland, P. R., & Price, S. F. (2012). Ice-shelf basal channels in a coupled ice/ocean model. *Journal of Glaciology*, **58**(212), 1227-1244.

Jakobsson, M., Mayer, L., Coakley, B., Dowdeswell, J. A., Forbes, S., Fridman, B., et al. (2012). The international bathymetric chart of the Arctic Ocean (IBCAO) version 3.0. *Geophysical Research Letters*, **39**(12).

Johnson, H., Münchow, A., Falkner, K., & Melling, H. (2011). Ocean circulation and properties in Petermann Fjord, Greenland. *Journal of Geophysical Research: Oceans*, **116**(C1).

Marshall, J., & Plumb, R. A. (2016). *Atmosphere, ocean and climate dynamics: an introductory text* (Vol. 21): Academic Press.

Morlighem, M., Rignot, E., Mouginot, J., Seroussi, H., & Larour, E. (2015). Icebridge bedmachine greenland, version 2. *NASA DAAC at the National Snow and Ice Data Center, Boulder, Colorado, USA (doi: 10.5067/AD7B0HQNSJ29)*.

Münchow, A., & Melling, H. (2008). Ocean current observations from Nares Strait to the west of Greenland: Interannual to tidal variability and forcing. *Journal of Marine Research*, **66**(6), 801-833.

Münchow, A., Melling, H., & Falkner, K. K. (2006). An observational estimate of volume and freshwater flux leaving the Arctic Ocean through Nares Strait. *Journal of Physical Oceanography*, **36**(11), 2025-2041.

Münchow, A., Padman, L., & Fricker, H. A. (2014). Interannual changes of the floating ice shelf of Petermann Gletscher, North Greenland, from 2000 to 2012. *Journal of Glaciology*, **60**(221), 489-499.

Münchow, A., Padman, L., Washam, P., & Nicholls, K. (2016). The Ice Shelf of Petermann Gletscher, North Greenland, and Its Connection to the Arctic and Atlantic Oceans. *Oceanography*, **29**(4), 84-95.

Padman, L., & Erofeeva, S. (2004). A barotropic inverse tidal model for the Arctic Ocean. *Geophysical Research Letters*, **31**(2).

Parker, B. B. (2007). *Tidal analysis and prediction*: US Department of Commerce, National Oceanic and Atmospheric Administration, National Ocean Service, Center for Operational Oceanographic Products and Services.

Pawlowicz, R., Beardsley, B., & Lentz, S. (2002). Classical tidal harmonic analysis including error estimates in MATLAB using T_TIDE. *Computers & Geosciences*, **28**(8), 929-937.

Persson, P.-O., & Strang, G. (2004). A simple mesh generator in MATLAB. *Siam Review*, **46**(2), 329-345.

Pritchard, H. D., Arthern, R. J., Vaughan, D. G., & Edwards, L. A. (2009). Extensive dynamic thinning on the margins of the Greenland and Antarctic ice sheets. *Nature*, **461**(7266), 971-975.

Rignot, E. (1996). Tidal motion, ice velocity and melt rate of Petermann Gletscher, Greenland, measured from radar interferometry. *Journal of Glaciology*, **42**(142), 476-485.

Rignot, E. (1998). Hinge-line migration of Petermann Gletscher, north Greenland, detected using satellite-radar interferometry. *Journal of Glaciology*, **44**(148), 469-476.

Rignot, E., & Steffen, K. (2008). Channelized bottom melting and stability of floating ice shelves. *Geophysical Research Letters*, **35**(2).

Schureman, P. (1958). *Manual of harmonic analysis and prediction of tides*: US Government Printing Office.

Segar, D. A. (2012) *Introduction to ocean sciences* (3th-First electronic edition ver 3.2 ed.).

Shepherd, A., Ivins, E. R., Geruo, A., Barletta, V. R., Bentley, M. J., Bettadpur, S., et al. (2012). A reconciled estimate of ice-sheet mass balance. *Science*, **338**(6111), 1183-1189.

Shroyer, E., Padman, L., Samelson, R., Münchow, A., & Stearns, L. (2017). Seasonal control of Petermann Gletscher ice-shelf melt by the ocean's response to sea-ice cover in Nares Strait. *Journal of Glaciology*, 1-7.

Sikirić, M. D., Janeković, I., & Kuzmić, M. (2009). A new approach to bathymetry smoothing in sigma-coordinate ocean models. *Ocean Modelling*, **29**(2), 128-136.

Straneo, F., & Heimbach, P. (2013). North Atlantic warming and the retreat of Greenland's outlet glaciers. *Nature*, **504**(7478), 36-43.

Straneo, F., Heimbach, P., Sergienko, O., Hamilton, G., Catania, G., Griffies, S., et al. (2013). Challenges to understanding the dynamic response of Greenland's marine terminating glaciers to oceanic and atmospheric forcing. *Bulletin of the American Meteorological Society*, **94**(8), 1131-1144.

Vaughan, D. G., Comiso, J. C., Allison, I., Carrasco, J., Kaser, G., Kwok, R., et al. (2013). Observations: cryosphere. *Climate change*, **2103**, 317-382.